

---

1 **This manuscript is a pre-print** and has been submitted for publication in **Tectonics**. This manuscript  
2 has not undergone peer-reivew. Subsequent versions of this manuscript may have different content. If  
3 accepted, the final version of this manuscript will be available via the “*Peer-reviewed Publication*  
4 *DOI*” link on the right hand side of this webpage. Please feel free to contact any of the authors directly  
5 or to comment on the manuscript using hypothes.is (<https://web.hypothes.is>). We welcome your  
6 feedback!

---

7

8      **Terrane boundary reactivation, barriers to lateral**  
9      **fault propagation and reactivated fabrics - Rifting**  
10     **across the Median Batholith Zone, Great South**  
11                    **Basin, New Zealand**

12      Thomas B. Phillips\*; Ken J. McCaffrey

13      *Department of Earth Sciences, University of Durham, Science labs, Elvet Hill, Durham, DH1 3LE*

14      *\*thomas.b.phillips@durham.ac.uk*

15      **Key points**

- 16            • We document multiple styles of structural inheritance influencing various aspects of rift  
17            physiography in the Great South Basin, New Zealand  
18            • The southern boundary of the Median Batholith Zone terrane is reactivated as a large  
19            extensional shear zone and detachment  
20            • Faults splay, segment and eventually terminate as they approach stronger material associated  
21            with a granitic laccolith.

22

## 23 **Abstract**

24 Prominent structural heterogeneities within the lithosphere may localise or partition strain and  
25 deformation during tectonic events. The NE-trending Great South Basin, offshore New Zealand,  
26 formed perpendicular to a series of underlying crustal terranes, including the dominantly granitic  
27 Median Batholith Zone, which along with boundaries between individual terranes, exert a strong  
28 control on rift physiography and kinematics. We find that the crustal-to-lithospheric scale southern  
29 terrane boundary of the Median Batholith Zone is associated with a crustal-scale shear zone that was  
30 reactivated during Late Cretaceous extension between Zealandia and Australia. This reactivated  
31 terrane boundary is oriented at a high-angle to the faults defining the Great South Basin. We identify a  
32 large granitic laccolith along the southern margin of the Median Batholith, expressed as sub-  
33 horizontal packages of reflectivity and acoustically transparent areas on seismic reflection data. The  
34 presence of this strong granitic body inhibits the lateral propagation of NE-trending faults, which  
35 segment into a series of splays that align along the margin as they approach. Further, we also identify  
36 two prominent E-W and NE-SW oriented fabrics within the basin, which are exploited by small-scale  
37 faults across the basin.

38 We show how different mechanisms of structural inheritance are able to operate simultaneously, and  
39 somewhat independently, within rift systems at different scales of observation. The presence of  
40 structural heterogeneities across all scales need to be incorporated into our understanding of the  
41 structural evolution of complex rift systems.

42

## 44 **1. Introduction**

45 Continental crust typically grows through the amalgamation of crustal terranes and the intrusion of  
46 igneous plutonic material. As a result, pre-existing structural heterogeneities are present throughout  
47 the lithosphere and exert a considerable influence over the development of rift systems across all  
48 scales. Individual crustal terranes contain numerous internal structural heterogeneities that reflect their  
49 unique tectonic histories, whilst the boundaries with adjacent terranes form pronounced crustal-to-  
50 lithosphere scale rheological and lithological contrasts (Howell 1980; McWilliams & Howell 1982;  
51 Bishop et al. 1985; Mortimer 2004; Lundmark et al. 2013; Peace et al. 2017; Johnston 2019).

52 Lithospheric-scale structures often localise strain, for example in orogenic belts surrounding cratonic  
53 continental interiors, and can control the location of rift systems and, to some extent, continental  
54 breakup (Wilson 1966; Dore et al. 1997; Tommasi & Vauchez 2001; Thomas 2006; Paton et al. 2016;  
55 Wenker & Beaumont 2016; Phillips et al. 2018; Thomas 2018; Heron et al. 2019). In rift systems, pre-  
56 existing structures in the crust may localise deformation and control the geometry and evolution of  
57 individual faults (Daly et al. 1989; Fossen et al. 2016; Mortimer et al. 2016; Phillips et al. 2016;  
58 Fazlikhani et al. 2017; Morley 2017; Peace et al. 2017; Dawson et al. 2018; Rotevatn et al. 2018b;  
59 Vasconcelos et al. 2019). Areas of stronger material, such as intruded plutons or stronger terranes may  
60 also inhibit fault nucleation and propagation, influencing the geometry of individual faults and the  
61 physiography of the overall rift (Critchley 1984; Koopmann et al. 2014; Magee et al. 2014; Peace et  
62 al. 2017; Howell et al. 2019). At the outcrop scale, pre-existing structures and fabrics may be  
63 exploited by later faults and fractures (Morley et al. 2004; Paton & Underhill 2004; De Paola et al.  
64 2005; Morley 2010; Chattopadhyay & Chakra 2013; Kirkpatrick et al. 2013; Duffy et al. 2015;  
65 Dichiarante et al. 2016; Mortimer et al. 2016; Phillips et al. 2017). This multitude of pre-existing  
66 structures exert a range of influences over extensional processes, however, an understanding of how  
67 these different structural heterogeneities are expressed in rift systems, how they link across scales and  
68 how they affect various aspects of rift physiography is currently lacking.

69 In this study, we focus on the Great South Basin, a NE-trending rift system located offshore the South  
70 Island of New Zealand. Basement beneath the basin comprises a series of volcano-sedimentary  
71 terranes, which accreted along the southern margin of Gondwana during protracted Cambrian-  
72 Cretaceous subduction (Mortimer et al. 1999; Tulloch et al. 1999; Mortimer 2004, 2014; Robertson et  
73 al. 2019; Robertson & Palamakumbura 2019; Tulloch et al. 2019). These terranes are separated by W-  
74 to WNW-trending crustal-to-lithospheric scale boundaries that are oriented perpendicular to the  
75 overlying basin (Muir et al. 2000; Mortimer et al. 2002). We focus on the evolution of the basin atop  
76 the Median Batholith Zone, a Carboniferous-Early Cretaceous Cordilleran-style magmatic arc, and its  
77 boundaries with the Western Province terranes to the south and the Brook Street and Murihiku  
78 Terranes to the north (Figure 1) (Bishop et al. 1985; Tulloch et al. 1999; Mortimer et al. 2002;  
79 Jongens 2006; Tulloch et al. 2019).

80 Based on borehole-constrained 2D and 3D seismic reflection data, we document multiple structural  
81 heterogeneities beneath the Great South Basin, and determine how they influence rift physiography  
82 and kinematics throughout multiple tectonic events. The framework provided by these pre-existing  
83 structures variably influences rift physiography across different scales of observation, from  
84 controlling rift segmentation and the location of sub-basins, to controlling the geometry and  
85 kinematics of individual fault systems.

86

## 87 **2. Regional geological setting and evolution**

88 The Great South Basin is a NE-trending rift basin located offshore of the east coast of the South  
89 Island of New Zealand. It contains a maximum sedimentary thickness of 8.6 km, which includes up to  
90 4 km of Upper Cretaceous strata (Beggs 1993; Sahoo et al. 2014; Morley et al. 2017) (Figure 1, 3).

91 The Great South Basin, along with the adjacent Canterbury Basin and Bounty Trough, is situated  
92 within the Campbell Plateau, a submerged (<1000 m water depth) area of thinned continental crust  
93 (~22 km) that extends ~1000 km southeast of the South Island (Figure 1) (Beggs 1993; Mortimer et  
94 al. 2002; Grobys et al. 2009; Uruski 2010; Higgs et al. 2019). Here, we focus on a 21,000 km<sup>2</sup> area

95 covering the southern part of the Great South Basin, located to the southeast of Stewart Island (Figure  
96 1).

97 The basement geology of New Zealand comprises a series of crustal to lithospheric terranes that  
98 accreted to the southern margin of Gondwana during protracted subduction from the Cambrian-Early  
99 Cretaceous (Bishop et al. 1985; Bradshaw 1989; Muir et al. 2000; Mortimer 2014). Subduction ceased  
100 during the Early Cretaceous (~105 Ma) as the buoyant Hikurangi Plateau collided along the margin  
101 (Davy et al. 2008; Uruski 2015). Since the Cenozoic, these terranes have been offset along the Alpine  
102 Fault, a major plate boundary and strike-slip fault located along the spine of the South Island that has  
103 accommodated ~480 km offset (Wellman 1953; Cooper et al. 1987; Sutherland et al. 2000). Due to  
104 this offset, the basement terranes of the South Island are also present beneath the North Island (Figure  
105 1) (Muir et al. 2000; Mortimer et al. 2002; Collanega et al. 2018). The basement terranes are divided  
106 into Eastern and Western provinces separated by the Median Batholith Zone. The timing of accretion  
107 along the Gondwana margin becomes younger eastwards, with those terranes of the Western Province  
108 terranes accreting to the margin of Gondwana earlier than those in the Eastern Province and  
109 occupying a more proximal position with respect to the continental interior. Here, we focus on those  
110 terranes that underlie the Great South Basin, the Western Province Terranes, the Median Batholith  
111 Zone and the Brook Street and Murihiku terranes of the Eastern Province (Figure 1).

112 The Western Province comprises the Buller and Takaka terranes, which represent a Gondwana-  
113 derived continental fragment accreted along the margin during the Cambrian-Devonian (Bradshaw  
114 1989; Mortimer 2004; Bache et al. 2014; Tulloch et al. 2019). The Eastern Province terranes largely  
115 originated within the Panthalassa Ocean as a series of volcanic and magmatic arcs and associated  
116 sedimentary basins (Bishop et al. 1985; Mortimer et al. 1997; Mortimer et al. 2002; Mortimer 2004).  
117 The Brook Street terrane is immediately north of the Median Batholith and comprises a Permian  
118 volcanic and volcanoclastic sequence that initially formed as an intra-oceanic arc (Landis et al. 1999;  
119 Mortimer 2004). Further north, the Murihiku terrane is composed of gently folded Jurassic-aged  
120 sandstones and volcanoclastic rocks that were initially part of a forearc sedimentary basin (Campbell  
121 et al. 2003; Mortimer 2004). Between the Western and Eastern Province terranes is the Median

122 Batholith Zone, a Cordilleran-style magmatic arc that represented the site of subduction-related  
123 magmatism from 375-110 Ma (Mortimer et al. 1999; Mortimer 2004). Although previously  
124 interpreted as a highly tectonised allocthonous zone, recent studies have demonstrated that the  
125 majority of plutonic material is autochthonous, with only relatively minor reworking and tectonism  
126 identified. Hence, we refer to the structure as the Median Batholith Zone (Mortimer et al. 1999). The  
127 Median Batholith Zone comprises numerous plutonic intrusions that can be divided into various suites  
128 based on the age of emplacement and composition (Tulloch 1988; Allibone & Tulloch 2004). An  
129 overall southwards younging trend occurs across the batholith (Mortimer et al. 1999; Allibone &  
130 Tulloch 2004), with the Cretaceous-aged Separation Point Batholith suite located along the southern  
131 margin of the zone and older batholith suites towards the northern margin (Muir et al. 2000; Allibone  
132 & Tulloch 2004).

133 The Great South Basin formed via two phases of extension during the Late Cretaceous related to the  
134 breakup of Gondwana. Extensional activity may have begun in the Jurassic-Early Cretaceous in a  
135 back-arc setting along the southern margin of Gondwana, with Jurassic strata identified in the  
136 deepwater Taranaki Basin and potentially in the Great South Basin (Grobys et al. 2007; Uruski et al.  
137 2007; Uruski 2010). Initial NE-SW oriented extension occurred between Australia and the contiguous  
138 Zealandia and Western Antarctica at ~101-89 Ma related to the opening of the Tasman Sea and the  
139 northwards propagation of the Tasman ridge (Kula et al. 2007; Kula et al. 2009; Sahoo et al. 2014;  
140 Tulloch et al. 2019). A second rift phase, related to the breakup of Zealandia and Western Antarctica  
141 and associated with the formation of the Pacific ridge, occurred at 90-80 Ma (Kula et al. 2007;  
142 Tulloch et al. 2019). Extensional stresses were oriented NW-SE, roughly parallel to the underlying  
143 basement terrane boundaries, and resulted in the formation of the NE-trending Great South Basin  
144 (Figure 1). Late Cretaceous extension, forming the Great South and Canterbury basins and the Bounty  
145 Trough greatly reduced the crustal thickness in the area to around 22 km (Mortimer et al. 2002). In the  
146 Great South Basin, faults related to this activity have been proposed to sole out onto a mid-crustal  
147 detachment (Uruski et al. 2007; Sahoo et al. 2014).

148 The onset of subduction in the Tonga-Kermadec region in the Oligo-Miocene and the formation of the  
149 Alpine Fault resulted in a regional compressional regime across New Zealand (Cooper et al. 1987;  
150 Sutherland et al. 2000; Sutherland et al. 2010; Bache et al. 2012). The Great South Basin was  
151 relatively far-removed from the compressional stresses associated with the formation of this new plate  
152 boundary, with regional compression expressed as low-amplitude, long wavelength folding (Uruski  
153 2010).

154

## 155 **3. Data and Methods**

### 156 **3.1 Seismic interpretation**

157 We use borehole-constrained 2D and 3D seismic reflection data, covering an area of 21,000 km<sup>2</sup>  
158 offshore of the South Island of New Zealand. A 3D seismic reflection volume (GSB-3D) was acquired  
159 in the south of this area and covers ~1,400 km<sup>2</sup> (Figure 1). Seismic reflection data follow the SEG  
160 normal polarity convention; that is, a downwards increase in acoustic impedance (i.e. the seabed) is  
161 represented by a peak, whereas a downwards decrease in acoustic impedance is represented by a  
162 trough (Figure 2). 2D seismic reflection data record to 6-8 s TWT and display variable image quality  
163 between individual surveys. The 3D seismic volume records to 8 s TWT and displays excellent image  
164 quality throughout.

165 The ages of regional stratigraphic horizons were constrained by the nearby Pukaki-1, Pakaha-1, Tara-  
166 1, Toroa-1 and Rakiura-1 boreholes (Figure 1). We mapped a series of prominent seismic reflections  
167 throughout the dataset and linked them to the regional stratigraphy (Figure 2). A seismic-well tie was  
168 performed on the Pukaki-1 well to link the seismic interpretations to the well data (Figure 2). A well-  
169 tie was not performed on the Pakaha-1 well due to a lack of coverage by wireline log data. Top  
170 Acoustic Basement and intra-Upper Cretaceous horizons form the main surfaces referred to  
171 throughout this study (Figure 2). Top Acoustic Basement typically represents top crystalline basement  
172 across the area (Figure 1), although in some instances, bedding-related reflectivity is observed beneath



173 this surface, potentially indicative of earlier activity (Figure 3). North of the study area, basement of  
174 the Murihiku terrane consists of allocthonous Permian to Early Cretaceous-aged sedimentary strata,  
175 where present these strata are classified as acoustic basement (Bache et al. 2014; Tulloch et al. 2019).  
176 The intra-Upper Cretaceous horizons was interpreted throughout the 3D seismic volume and across  
177 the main basin depocentre to map syn-rift fault geometries in more detail (Figure 1, 3). Shallower  
178 horizons are also interpreted in the post-rift interval, although these provide little information on the  
179 structural evolution of the basin (Figure 2, 3). Seismic interpretations were carried out, and are  
180 presented, in the time domain (seconds Two-way-travel time; s TWT). Key structural measurements  
181 were converted to the depth domain based on regional checkshot information.

182 Crystalline basement in the area is mostly associated with the underlying Median Batholith (Figure 1).  
183 The Pakaha-1 well penetrates a granitic basement dated at ~323 Ma that is interpreted to represent  
184 Carboniferous basement to the Median Batholith (Figure 4) (Tulloch et al. 2019). The Pukaki-1 well  
185 penetrates further granitic basement to the southeast (Figure 1). This granite is dated at 107 Ma and  
186 can be confidently correlated with the Separation Point Batholith suite (Tulloch et al. 2009; Tulloch et  
187 al. 2019). The Separation Point Batholith suite is also identified in the same structural setting, along  
188 the boundary between the Median Batholith and Western Province terranes, in the North Island (Muir  
189 et al. 2000).

## 190 **3.2 Quantitative fault analysis**

191 We performed quantitative analyses, in the form of throw-length plots, on a series of faults within the  
192 basin to quantify their geometric and kinematic evolution. The geometry of each fault analysed,  
193 including horizon cutoffs and any tip lines were carefully constrained throughout the data to minimise  
194 any interpretation-related artefacts (Walsh et al. 2003; Duffy et al. 2015). Based on our fault  
195 interpretations we calculated throw-length plots for individual fault segments at both the Acoustic  
196 Basement and intra-Upper Cretaceous stratigraphic horizons. To accurately constrain the kinematic  
197 evolution of a fault we need to record all fault slip-related strain, including both brittle faulting and  
198 ductile folding such as that associated with fault propagation folding. Therefore, horizon cut-offs were

199 projected to the fault plane from an area unaffected by local fault parallel folding (Walsh et al. 1996;  
200 Long & Imber 2012; Whipp et al. 2014; Duffy et al. 2015; Coleman et al. 2018)

201 Throw measurements were taken along a series of parallel seismic sections oriented orthogonal to the  
202 main fault trend, each separated by ~339 m. Analyses of individual faults were then collapsed onto a  
203 single plane representing a strike projection of the overall fault system. This allowed us to calculate  
204 the cumulative throw accrued across the fault system and to analyse how strain was accommodated  
205 along its length.

206

## 207 **4. Rift physiography**

208 In this section, we describe the overall rift physiography of the study area. We first describe the  
209 regional geometry of the Great South Basin across the Acoustic Basement surface, before describing  
210 the detailed fault and rift geometry, at both the Acoustic Basement and intra-upper Cretaceous  
211 structural levels, using the 3D seismic volume in the centre of the basin (Figure 1).

### 212 **4.1 Regional rift geometry**

213 The Great South Basin is characterised by NE-trending, predominantly SE-dipping faults. NW-  
214 dipping faults are also present and help define a series of NE-trending basement ridges in the east of  
215 the area (Figure 1). The centre of the basin reaches 3-4 s TWT (~4.5 km) depth and shallows  
216 eastwards onto the continental shelf (~1.5 s TWT, ~1.3 km) (Figure 1, 3). The basin deepens to  
217 around 5 s TWT (~9 km) in the north and the south (Figure 1).

218 Upper Cretaceous syn-rift strata thicken into the hangingwalls of major NE-trending faults (Figure 3),  
219 indicating Late Cretaceous activity along these structures. We also recognise a potentially earlier  
220 phase of activity, with apparent syn-rift strata present below the acoustic basement surface in the  
221 hangingwalls of some structures (Figure 3). Although we are unable to assign an age to these strata,  
222 we suggest that, based on regional considerations, they are likely Late Jurassic-Cretaceous in age

223 (Uruski et al. 2007; Uruski 2010). Palaeocene to recent strata comprise the post-rift basin fill and  
224 display a slight westwards thickening related to increased sediment input and clinoform progradation  
225 from the mainland (Figure 3). A large clinoform sequence at the seafloor forms a major bathymetric  
226 escarpment to the west (Figure 3). E-dipping faults along the western margin of the basin appear to  
227 merge at depth, potentially reflecting the listric geometry observed elsewhere (Uruski et al. 2007)  
228 (Figure 3). In the east of the area, the Pakaha-1 well penetrates granitic basement atop a ~10 km wide  
229 NE-trending horst termed the Pakaha Ridge (Figure 1). Basement beneath this ridge is highly  
230 reflective and appears to dip westwards. A series of W-dipping faults define the western margin of  
231 this ridge and appear to merge with the basement reflectivity at ~5-6 s TWT (~10.5 km) (Figure 3).  
232 A major WNW-trending, SSW-dipping fault is identified in the south of the area, and is associated  
233 with a large WNW-ESE oriented depocentre (~5 s TWT; 9 km depth) in its hangingwall (Figure 1).  
234 This structure is co-located with the boundary between the Median Batholith Zone and the Western  
235 Province Terranes, and is henceforth termed the Terrane Boundary Fault (Figure 1). A WNW-  
236 trending structural high is present in the footwall of the Terrane Boundary Fault, defining a relatively  
237 unfaulted area bound to the south by the Terrane Boundary Fault and to the north by WNW-trending,  
238 NE-dipping faults (Figure 1, 4a). The structural high appears to link into the Pakaha ridge to the east.  
239 We henceforth refer to this structural high as the Terrane Boundary Fault (TBF) Footwall Block  
240 (Figure 1, 4).

## 241 **4.2 Detailed basin geometry – 3D seismic volume**

242 Two horizons mapped through the 3D seismic volume provide additional detail on the fault  
243 geometries and rift physiography in the centre of the basin (Figure 4). Two NE-striking, SE-dipping  
244 faults are present at the Acoustic Basement surface in the north of the area (Figure 4a). The  
245 northernmost fault forms the northern boundary to the main basin depocentre (Figure 1, 3, 4a). The  
246 other fault forms a single structure in the northeast that splays into series of smaller segments to the  
247 southwest and is referred to as the ‘Splaying Fault System’. Individual segments of the Splaying Fault  
248 System dip southeast and northwest, resulting in complex plan-view geometries and non-resolvable

249 cross-cutting relationships at depth (Figure 3, 4a). As they approach the northern margin of the TBF  
250 Footwall Block in the southwest, the segments rotate around vertical axes to a more WNW orientation  
251 and terminate along the boundary of the TBF Footwall Block (Figure 4). The TBF Footwall Block  
252 itself is relatively unfaulted; with only a few minor WNW- and NE-trending faults present (Figure  
253 4a). Although the northern margin of the TBF Footwall Block is largely parallel to the Terrane  
254 Boundary Fault, a series of embayments are present along its southern margin, in the immediate  
255 footwall of the fault (Figure 4a). These embayments are typically 5-8 km wide and incise about ~6 km  
256 back into the TBF Footwall Block.

257 The complex geometry of the Splaying Fault System is further highlighted across the intra-Upper  
258 Cretaceous surface (Figure 4b). The footwall of the main fault is cross-cut by a series of SE and NW-  
259 dipping faults to the southwest, with some NW-dipping antithetic faults also developing in the  
260 hangingwall. Individual segments of the Splaying Fault system rotate to a more WNW-trending  
261 orientation as they approach the TBF Footwall Block (Figure 4b). Horsetail splay geometries are  
262 identified along-strike of the main fault, where both NW- and SE-dipping fault segments diverge and  
263 rotate to become NE-dipping (Figure 4b).

264 Some NE-striking, SE-dipping faults are present to the southwest of the area, defining a series of NE-  
265 trending structural highs superimposed atop the TBF Footwall Block (Figure 4b). The Terrane  
266 Boundary Fault is not clearly expressed at this structural level, although a few minor WNW-trending,  
267 SSW-dipping faults are present along the southern margin of the WNW-block (Figure 4b).

## 268 **5. Styles of structural inheritance**

### 269 **5.1 Terrane boundary reactivation**

270 The Terrane Boundary Fault forms a ~65 km long structure across the southern margin of the area and  
271 is coincident with the boundary between the Median Batholith Zone and the Western Province  
272 terranes (Figure 1). The fault dips SSW, away from the Median Batholith Zone, and records >1 s (>2  
273 km) of throw across the Acoustic Basement surface (Figure 5, 6).

274 The Terrane Boundary Fault corresponds to a prominent reflection on seismic data, with a package of  
275 high-amplitude inclined reflections present in its footwall. This package of reflections is truncated by  
276 the top Basement surface and extends to lower crustal depths (8 s TWT; ~20 km) (Figure 5, 6).  
277 Internal reflections are remarkably continuous within the package, spanning depth intervals of >2.5 s  
278 (Figure 5). The width of the reflection package increases at shallower depths, from ~2 km wide at 6-7  
279 s TWT (~15 km), to ~5 km wide at 2-3 s TWT (~2.7 km) (Figure 5, 6). A reflection corresponding to  
280 the lower boundary of this package can be traced to the top Acoustic Basement surface, where the  
281 package delineates a 5-7 km wide subcrop at the top Acoustic Basement surface (Figure 5).

282 A series of faults merge with the Terrane Boundary Fault downdip, defining a series of fault blocks  
283 that show increasing offset along the fault with depth (Figure 5). The timing of activity along these  
284 faults appears to migrate updip along the structure, with deeper faults showing earlier activity than  
285 those at shallow depths (Figure 5). In some areas, the fault plane becoming sub-horizontal at  
286 shallower depths, creating a series of embayments that extend northwards into the footwall of the  
287 Terrane Boundary Fault and the TBF Footwall Block (Figure 4, 7). Fault blocks within these  
288 embayments detach onto the top reflection of the reflection package and show south-directed transport  
289 downdip (Figure 6, 7).

290 In addition to the inclined reflection package associated with the footwall of the Terrane Boundary  
291 Fault, we also observe packages of high-amplitude reflectivity at mid-crustal depths (4-6 s TWT; 6-12  
292 km) which extend beneath the TBF Footwall Block. These reflection packages are typically sub-  
293 horizontal although they may dip slightly northwards further to the north (Figure 5, 6). Beneath the  
294 platform to the west, these reflection packages define areas of high- and low-reflectivity within  
295 crystalline basement that extend from 3-6 s TWT (3.5-12.5 km) (Figure 5). Beneath the basin, the  
296 packages display a more domal geometry and are present from 5-7 s TWT (9-16.5 km) (Figure 6). In  
297 both instances, the packages merge with those associated with the Terrane Boundary Fault and are  
298 only present in its footwall.

299 Based on its geometry and seismic reflection character, we interpret the high-amplitude and coherent  
300 package of intra-basement reflectivity in the footwall of the Terrane Boundary Fault as representing a

301 shear zone (termed the Terrane Boundary Shear Zone). The seismic character of the intrabasement  
302 reflectivity resembles that of shear zones identified elsewhere in seismic data. In these other  
303 examples, the shear zone interpretation can be independently verified through links to structures  
304 identified onshore (Freeman et al. 1988; Wang et al. 1989; Phillips et al. 2016; Fazlikhani et al. 2017;  
305 Lenhart et al. 2019) or encountered in boreholes (Hedin et al. 2016). The characteristic intra-basement  
306 reflectivity forms through constructive interference between highly deformed mylonite zones and  
307 intervening relatively undeformed material (Jones & Nur 1984; Carreras 2001; Reeve et al. 2013;  
308 Rennie et al. 2013; Phillips et al. 2016). We interpret the prominent reflection at the top of the shear  
309 zone as a detachment horizon, potentially exploiting a relatively weak mylonitic zone.

310 We interpret the sub-horizontal reflection packages in the footwall of the Terrane Boundary Shear  
311 Zone to represent a series of granitic laccolith intrusions. Granitic material is present in this area due  
312 to our location within the Median Batholith Zone (Mortimer et al. 1999; Tulloch et al. 2019). Our  
313 interpretation is further corroborated by granitic basement in the nearby Pakaha-1 and Pukaki-1  
314 boreholes (Figure 1). In addition, the reflection character within basement of the likely granitic  
315 Pakaha Ridge resembles that identified here (Figure 3, 6), with the Pakaha Ridge also potentially  
316 joining with the TBF Footwall Block in the east of the area (Figure 1). Granitic plutons belonging to  
317 the Separation Point Batholith suite are identified between the Western Province Terranes and the  
318 Median Batholith Zone beneath the Taranaki Basin, offshore of the North Island (Mortimer et al.  
319 1997; Muir et al. 2000). Furthermore, the reflection patterns observed here, of sub-horizontal  
320 packages of high- and low- amplitude packages of reflectivity, resemble those observed from the Lake  
321 District Batholith, where prominent reflections are generated at the boundaries of stacked granite  
322 laccoliths (Figure 5) (Evans et al. 1993; Evans et al. 1994). The interpreted reflection packages also  
323 display a lenticular geometry, consistent with those expected from granitic intrusions (McCaffrey &  
324 Petford 1997; Petford et al. 2000). At the top Acoustic Basement structural level, this granite  
325 underpins the relatively unfaulted TBF Footwall Block (Figure 4). In the platform area, a prominent  
326 package of reflections at ~6 s TWT (~12 km) depth may be interpreted as the base of the granite  
327 batholith, with the lenticular granite bodies extending upwards to ~3 s TWT (~3.5 km) (Figure 5).

328 Further east, the top of the granitic body appears to be situated at shallower depths (~5 s TWT; ~9  
329 km) (Figure 6).

## 330 **5.2 Strong crustal blocks as barriers to fault propagation**

331 As outlined in the previous section, we propose that a granitic body (Figure 3) underlies the relatively  
332 unfaulted TBF Footwall Block. To the north, the NE-trending Splaying Fault System abuts against  
333 and terminates at the Footwall Block to the southwest (Figure 4). Reflectivity associated with the NE-  
334 trending Splaying Fault systems cross-cuts the granite-related reflectivity in the footwall of the  
335 Terrane Boundary Fault, indicating that activity along the Splaying Fault system occurred after the  
336 Footwall block was established (Figure 6, 7). We now describe in detail how the geometry of the  
337 Splaying Fault System changes from NE to SW, towards the TBF Footwall Block.

338 In the northeast of the area, away from the TBF Footwall Block, strain is accommodated by a single  
339 fault (Figure 8a). Evidence of earlier activity is also present in this area, with the identification of  
340 bedding- and fault-related reflectivity beneath the Acoustic Basement surface (Figure 8a). Any pre-  
341 Acoustic Basement strata is likely to be Jurassic to Early Cretaceous in age, relating to the earliest  
342 stages in the basin's formation (Uruski et al. 2007; Uruski 2010). Approaching the WNW-trending  
343 TBF Footwall Block to the southwest, the fault begins to splay into a series of SE- and NW-dipping  
344 faults synthetic and antithetic to the main fault respectively (Figure 4b, 8b). This fault segmentation is  
345 initially accommodated by dissection of the footwall into four fault segments that merge to a single  
346 structure at depth, and by the formation of a series of antithetic faults in the hangingwall (Figure 8b).  
347 The antithetic faults also appear to abut against the main fault structure at depth, although detailed  
348 cross-cutting relationships cannot be identified in the data. Additional NW-dipping faults form in the  
349 footwall of the main fault, dipping away from the structure and further bisecting the footwall (Figure  
350 8b). As the fault continues to the southwest, the footwall becomes very highly deformed by both SE-  
351 and NW-dipping faults such that no dominant fault or overall hangingwall and footwall can be  
352 identified (Figure 8c). At this distance along the fault, extension is accommodated by multiple faults  
353 across a ~15 km wide zone (Figure 8c). Pre-acoustic basement sedimentary strata are again identified

354 in this area, although no divergent stratal wedges are identified in the hangingwalls of the segments of  
355 the Splaying Fault, indicating that it was not active at that time (Figure 8c). However, we do identify  
356 pre-acoustic basement syn-rift strata in the hangingwalls of the major faults to the northwest and  
357 southeast of the Splaying Fault system (Figure 8a, 8b). As the Splaying Fault System approaches the  
358 TBF Footwall Block, extension is accommodated by a complex system of NW- and SE dipping faults  
359 (Figure 8d). The dominant fault appears to switch in this location, with a NW-dipping fault seemingly  
360 cross-cutting the SE-dipping fault that is dominant along-strike to the northeast (Figure 8d). The main  
361 segments of the splaying fault begin to rotate to a WNW-striking orientation, dipping to the northeast  
362 (Figure 4b). The rotation of these faults appears to be at least partially accommodated by the upwards  
363 splaying of the faults (Figure 8d). A series of NW-dipping faults to the east of the Splaying Fault  
364 merge into a package of reflectivity at depth and join with an additional fault to the east that forms the  
365 border to a basement ridge (Figure 4, 8d). The geometry and structural style of these faults resemble  
366 those along the western border of the Pakaha ridge, where multiple faults root onto the margin of a  
367 granitic basement ridge (Figure 3, 8d).

368 By measuring throw across individual segments within the Splaying Fault System we are able to  
369 quantitatively analyse how strain is accommodated along the length of the fault; from the single  
370 structure in the northeast, to the wider zone of deformation proximal to the TBF Footwall Block in the  
371 southwest. In the northeast, throw across both the Acoustic Basement and Intra-upper Cretaceous  
372 surfaces is accommodated by a single fault, accounting for ~800 ms (~1.8 km) and ~250 ms (~200 m)  
373 throw across each surface respectively (Figure 9, 10). Two throw minima are present along the throw  
374 profile, corresponding to bends in the fault trace and representing relay ramps along the fault (Figure  
375 4, 9). Throw across the top Acoustic Basement surface decreases to the southwest at around 15 km  
376 along the fault, as extension is accommodated by a series of smaller segments in the footwall and  
377 hangingwall, each accommodating 100-200 ms throw (~200 m) (Figure 9). One notable feature is that  
378 as the fault splays and the dominant fault in the northeast terminates, the cumulative throw across the  
379 whole system remains relatively constant. To the southwest, extension is accommodated by more  
380 numerous, lower displacement segments (Figure 9). The relatively constant cumulative throw along



381 the system indicates that the strain and applied stress is constant along the length of the fault and that  
382 the degree of maturity of the fault is not responsible for its segmentation and splaying geometry (cf.  
383 Nixon et al. 2014).

384 A cumulative throw minimum is present at ~24 km along the length of the fault at the Acoustic  
385 Basement structural level. However, this appears to be related to a lack of imaging of faults in this  
386 area rather than a property of the system itself (Figure 9). To the southwest, the individual fault  
387 segments rotate to a more WNW-orientation and terminate at the northern margin of the TBF  
388 Footwall Block (Figure 4a). At the boundary of the TBF Footwall Block, cumulative throw decreases  
389 from ~600 ms to zero over a distance of ~1 km, leading to a large gradient in the cumulative fault  
390 throw.

391 Throw analyses across the Intra-upper Cretaceous surface tell a similar story to the Acoustic  
392 Basement surface (Figure 10). Individual fault segments are better resolved across this surface  
393 meaning that they may provide a more complete record of the distribution of strain along the Splaying  
394 Fault system (Figure 10). As across the Acoustic Basement surface, throw is initially accommodated  
395 by a single, segmented fault in the northeast (Fault 1; Figure 10), which records 250-350 ms (~250 m)  
396 throw. To the southwest, throw across this fault drastically decreases with throw being accommodated  
397 by at least 20 smaller segments. At around 11 km along the Splaying Fault system, a new fault (F2;  
398 Figure 10) forms in the hangingwall of Fault 1 and initially accommodates around ~150 ms (~200 m)  
399 throw compared to 25-50 ms (~50 m) throw across Fault 1 in the same location. In the northeast, Fault  
400 1 appears to have been associated with a period of fault propagation folding prior to the brittle offset  
401 of the intra-upper Cretaceous surface, which is incorporated into our throw analyses (Figure 8a).  
402 When F2 forms in the hangingwall of Fault 1, it records the ductile deformation rather than Fault 1,  
403 now located in the footwall of F2 (Figure 10). Further southwest, extension is accommodated by  
404 multiple, low-displacement splays (~50 ms throw), which produce a relatively constant cumulative  
405 throw across the whole Splaying Fault System (~200 ms) (Figure 10). In contrast to the Acoustic  
406 Basement surface, we do not identify a prominent minimum along the fault splays (~24 km) (Figure  
407 10). As the Splaying Fault system approaches the northern margin of the TBF Footwall Block,

408 individual segments begin to rotate to align with the margin and terminate (Figure 4b, 10). At the  
409 northern margin of the TBF Footwall Block, cumulative throw across the system decreases from ~150  
410 ms to ~50 ms over a distance of 1-2 km, forming a relatively high displacement gradient (Figure 10).  
411 Some low-displacement faults (~20 ms throw) propagate into the TBF Footwall Block (Figure 10).

412 In the northeast, the Splaying Fault System is characterised by a singular fault plane, resembling a  
413 relatively typical fault associated with Late Cretaceous rifting in the Great South Basin (Uruski et al.  
414 2007; Sahoo et al. 2014). No major faults are present across the TBF Footwall Block to the southwest.  
415 As the Splaying Fault approaches this block it begins to splay into a series of relatively low-  
416 displacement segments. Those segments emanating from the footwall of the main fault display a  
417 divergent geometry, dipping away from the main fault, whereas those in the hangingwall appear to  
418 form a more convergent geometry (Figure 4, 10). We propose that the granite-cored TBF Footwall  
419 Block represents an area of stronger material that inhibits fault nucleation and acts as a barrier to  
420 lateral fault propagation.

421 We observe complex fault geometries along the northern margin of the TBF Footwall Block (Figure  
422 11). Horsetail splay type geometries are situated at the terminations of Faults 15 and 16 across the  
423 intra-upper Cretaceous surface (Figure 11). NE trending faults rotate sharply to NW and S/SE  
424 orientations at the boundary of the TBF Footwall Block, whilst also splaying into a series of segments  
425 that define small-scale graben structures (Figure 11). The graben structures are oriented parallel to the  
426 northern margin of the TBF Footwall Block and seemingly parallel to the prevailing extension  
427 direction (Figure 11). Faults defining these graben appear to originate from a single point located at a  
428 deeper structural level and are only expressed across the intra-upper Cretaceous surface (see inset on  
429 Figure 11). We interpret that these graben form as a consequence of the fault trying to reduce throw  
430 and terminate, in the presence of a barrier to further lateral propagation. In addition, stress  
431 perturbations proximal to the margin of the granitic TBF Footwall Block may have locally influenced  
432 the rotated WNW-ESE striking faults (Figure 11) (cf. Morley 2010; Rotevatn et al. 2018b). Some NE-  
433 trending faults are identified to the south west of the horsetail splay faults (i.e. Faults 17 and 20 in  
434 Figure 11), forming E-W to NE-SW trending grabens. We suggest that these relatively low-

435 displacement faults broke through the initial barrier to propagation following an initial period of  
436 retardation at the TBF Footwall Block (Figure 11).

### 437 **5.3 Reactivation of basement fabrics**

438 We identify two prominent basement fabrics across the Great South Basin, dipping towards the south  
439 (Figure 12) and to the east (Figure 13). These fabrics are also associated with faults that offset the top  
440 Acoustic Basement horizon and align with the fabric in basement (Figure 12, 13). The fabrics are  
441 characterised by relatively linear dipping packages of reflections within basement, often truncated at a  
442 high angle by the top Acoustic Basement surface. The fabrics often mutually cross-cut oppositely-  
443 dipping basement reflections and display small-scale (~1 km wide), high-amplitude reflections in  
444 these areas (Figure 12, 13). Additional basement reflectivity, associated with the Terrane Boundary  
445 shear zone and the granitic body, is also present throughout the area but is distinct from these  
446 basement fabrics (Figure 12).

447 The basement fabrics are developed throughout the study area but are most pronounced across the  
448 granitic footwall block of the Terrane Boundary Fault, where they are shown to be associated with an  
449 E-W trending and a NE-SW trending fault population across the Acoustic Basement surface (Figure  
450 14). At first glance, the different fabrics appear to display mutually cross-cutting relationships, with  
451 no ability to distinguish relative timing of formation (Figure 5, 6). However, the NE-SW fabric  
452 appears to offset the E-W fabric in some areas; in addition, the NE-SW fabric also appears to abut  
453 against the fabric rather than be offset by it (Figure 14), although this relationship is not clear.  
454 However, in cross-section, we observe that the fabrics associated with the NE-trending faults offset  
455 the E-W striking fabrics associated with the shear zone (Figure 7), indicating that the NE-SW fabric  
456 postdates the E-W fabric (Figure 14).

457 The E-W fabric aligns with and shares a similar S-dipping geometry as the Terrane Boundary Fault  
458 and shear zone. This fabric does not appear to be related to the NE-trending faults within the basin,  
459 including the Splaying Fault system, which cross-cut the fabric (Figure 12). The NE-SW fabric is  
460 aligned with, and displays a similar dip to, the NE-trending fault population.

461 Prominent fabrics as observed on seismic reflection data may be related to a number of different  
462 features including sedimentary strata, fault plane reflections, highly foliated basement rocks and shear  
463 zones (Phillips et al. 2016; Fazlikhani et al. 2017; Lenhart et al. 2019) and dyke swarms (Abdelmalak  
464 et al. 2015; Phillips et al. 2017). The E-W fabric appears to be associated with the Terrane Boundary  
465 Fault and associated shear zone, appearing to link with the structure to the south (Figure 12). This  
466 fabric may therefore represent shear-related fabrics within the granitic block, exploited by multiple  
467 low-displacement faults. This generation of this fabric may relate to an early phase of activity within  
468 the Great South Basin, potentially related to the early stages of the separation of Zealandia and  
469 Australia (Kula et al. 2007; Tulloch et al. 2019), or extension within a back-arc setting (Uruski 2010).

470 The NE-SW fabric appears to be related to NE-trending faults formed due to NW-SE oriented  
471 extension associated with formation of the Great South Basin and the separation of Zealandia and  
472 Western Antarctica (Kula et al. 2007; Sahoo et al. 2014; Tulloch et al. 2019). Faults associated with  
473 this extension are proposed to link to a detachment at mid-crustal depths (Uruski et al. 2007). We  
474 suggest that this fabric may relate to hangingwall flexure associated with this activity. Alternatively,  
475 in some areas the fabric may also represent the rotated sedimentary bedding-related reflectivity from  
476 an earlier rift phase. Although this doesn't match the with the relationship between the main E-  
477 dipping fabric and faults shown in Figure 13, it may be associated with a fault out of the plane of the  
478 section. In this instance, the rotated bedding-related reflectivity may be exploited by faults during  
479 later hangingwall flexure (Figure 13).

480

## 481 **6. Discussion**

### 482 **6.1 Terrane boundary reactivation and the regional evolution of** 483 **the Great South Basin**

484 The Great South Basin formed perpendicular to the boundaries between a series of basement terranes  
485 accreted along the southern margin of Gondwana during a protracted period of subsidence (Beggs

486 1993; Mortimer et al. 2002). Following Cenozoic-to-recent activity along the Alpine Fault (Cooper et  
487 al. 1987; Cooper & Norris 1994; Sutherland et al. 2000), the terranes underlying the Great South  
488 Basin are also present offshore North Island, beneath the Taranaki Basin (Muir et al. 2000; Collanega  
489 et al. 2018). Regional seismic data indicates that the boundaries between individual terranes extend  
490 throughout the crust, and likely the lithosphere (Muir et al. 2000; Mortimer et al. 2002).

491 We identified in this study a major crustal-scale shear zone and associated upper-crustal fault system  
492 between the Median Batholith and Western Province terranes, representing a reactivation of the  
493 terrane boundary (Figure 5, 6). To the north, in the Taranaki Basin, the boundary between these  
494 terranes was initially exploited by the intrusion of the Separation Point Batholith suite, with the Cape  
495 Egmont Fault zone then exploiting the boundary between the Separation Point and Median batholiths  
496 (Muir et al. 2000; Collanega et al. 2018). In this instance, the terrane boundary appears to have also  
497 been initially exploited by granitic bodies belonging to the Separation Point Batholith suite, as also  
498 sampled along strike in the Pukaki-1 well. Subsequently, this terrane boundary is later reactivated,  
499 with the formation of a shear zone along the margin of the granite (Figure 15, 16). The localisation of  
500 the shear zone along the margin of the granitic body may explain why the shear zone thins with depth.  
501 At deeper levels the shear zone is pinned along the margin of the granite, whereas at shallower  
502 basement levels, where the granite may be absent, the shear zone is less confined. The prominent  
503 contrast in lithological properties between the Median Batholith, including the Separation Point  
504 Batholith suite, and the Western Province terranes localised strain and led to reactivation of the  
505 terrane boundary (Figure 15).

506 The WNW-trending Terrane Boundary Fault is oriented at a high angle to the NE-trending faults of  
507 the Great South Basin (Figure 1). Whilst it is possible that local stress perturbations relating to pre-  
508 existing structures led to the development of non-optimally oriented structures (Morley 2010;  
509 Philippon et al. 2015; Phillips et al. 2016; Rotevatn et al. 2018b; Samsu et al. 2019), we do not think  
510 that this is the case due to the high angle between the structures. Instead, we propose that these non-  
511 collinear structures formed during multiple phases of extension relating to the multiphase breakup of  
512 Gondwana in the Late Cretaceous (Kula et al. 2007; Tulloch et al. 2019). Based on geometric

513 relationships between the NE- and E- basement fabrics (Figure 7, 14, 15c), we suggest that the WNW-  
514 trending structures formed prior to the NE-trending faults and fabrics. An initial phase of extension  
515 occurred at 100-90 Ma, related to the breakup between Australia and the contiguous Zealandia and  
516 Western Antarctica. Offshore of the southeast South Island, the extension direction was oriented  
517 roughly NE-SW (Tulloch et al. 2019), with the boundaries between basement terranes, representing  
518 crustal-scale weaknesses that were optimally oriented to be reactivated during this phase of extension.  
519 We suggest that this initial phase of extension was responsible for the formation of the Terrane  
520 boundary shear zone and associated fault. This phase of activity was also associated with activity  
521 across the Sisters Shear Zone, onshore Stewart Island (Kula et al. 2009). Although the WNW-trending  
522 Terrane Boundary shear zone is oblique to the NE-trending Sisters Shear Zone, it is aligned with the  
523 Gutter Shear zone and the Freshwater and Escarpment fault systems, which show dextral  
524 transpressional activity during the Early Cretaceous (Allibone & Tulloch 2004, 2008). While some  
525 oblique slip is possible along the Terrane Boundary Fault, this would not appear to be the case based  
526 on the SSW-directed transport of footwall blocks and the orientation of the embayments (Figure 4, 7).  
527 Therefore, we suggest that the geometry of the Terrane Boundary Shear zone was controlled by the  
528 granite body, and therefore not aligned with the Sisters shear zone.

529 Following breakup between Australia and Zealandia, a second phase of rifting occurred from ~90-80  
530 Ma and was related to the breakup of Zealandia and Western Antarctica, leaving Zealandia as an  
531 isolated continent. This phase of extension was oriented NW-SE and resulted in the formation of NE-  
532 trending faults across the Great South Basin and thinning of the crustal thickness to ~22 km (Beggs  
533 1993; Uruski et al. 2007; Grobys et al. 2009; Sahoo et al. 2014). This phase of activity was oriented at  
534 a high angle to the WNW-trending Terrane boundary, which was therefore not reactivated. However,  
535 the Terrane boundary shear zone, and the granitic body in its immediate footwall, blocked the lateral  
536 propagation of faults and segmented the rift (Figure 15b) (Dore et al. 1997; Corti 2008; Koopmann et  
537 al. 2014; Henstra et al. 2015; Peace et al. 2017; Heilman et al. 2019).

## 538 **6.2 3D geometry and seismic expression of a granitic batholith**

539 Although the Median Batholith represents a large area of igneous material, it is by no means a  
540 homogeneous body. The batholith is a composite structure formed during a protracted period of  
541 magmatism and comprises multiple generations of plutonic material with complex overprinting  
542 relationships as observed onshore (Mortimer et al. 1999; Allibone & Tulloch 2004). The large,  
543 composite nature of the Median Batholith resembles other batholiths worldwide, such as the  
544 Cordillera Blanca batholith of the Peruvian Andes (Petford & Atherton 1992) and the North American  
545 Sierra Nevada Batholith (Schwartz et al. 2014).

546 We suggest the granitic body underpinning the TBF Footwall Block belongs to the Cretaceous-aged  
547 Separation Point Batholith Suite. Intrusions displaying Separation Point affinity have been identified  
548 along the same terrane boundary in the Taranaki Basin (Mortimer et al. 1997; Muir et al. 2000), and  
549 form the basement of the Pukaki-1 well, which is also situated along the footwall of the Terrane  
550 Boundary Fault (Figure 1) (Tulloch et al. 2019). Late Early Cretaceous batholiths along-strike to the  
551 northwest on Stewart Island are largely confined to the south of the Gutter Shear zone, towards the  
552 boundary with the Western Province terranes (Mortimer et al. 1999; Allibone & Tulloch 2004). The  
553 Separation Point suite was intruded into Carboniferous-aged plutons, such as those penetrated in the  
554 Pakaha-1 well (Figure 1) (Tulloch et al. 2019). The spatial relationships between the granitic bodies  
555 offshore resembles those observed onshore Stewart Island (Allibone & Tulloch 2004).

556 Due to their relatively homogeneous nature, granitic bodies do not generate prominent impedance  
557 contrasts and often appear acoustically transparent on seismic reflection data. However, reflections  
558 can be generated at contacts between the granitic body and surrounding country rock, giving us  
559 insights into the gross granite morphology. Seismic reflections have previously been identified  
560 originating from the top and base of granitic bodies (Lynn et al. 1981; McLean et al. 2017; Howell et  
561 al. 2019), as well as from internal fractures (Mair & Green 1981) and layered granitic laccoliths  
562 (Evans et al. 1993; Evans et al. 1994). When observed in seismic data, granitic intrusions typically  
563 display a laccolith-style geometry, consisting of stacked, lenticular bodies (Lynn et al. 1981; Evans et  
564 al. 1994; McCaffrey & Petford 1997; Petford et al. 2000). Beneath the TBF Footwall Block, we  
565 observe layered and domal packages of reflections, resembling laccolith style geometries (Figure 5, 6,

566 15a), whereas across the TBF Footwall Block itself we identify some areas displaying relatively  
567 acoustically transparent seismic facies (Figure 12, 13). These acoustically transparent areas in some  
568 places may be cross-cut by shear zone-related reflectivity, potentially corresponding to faults and  
569 fractures within the granite itself (Figure 12).

570 The geometry of the interpreted granite body shows some variability along-strike and is not at a  
571 constant depth beneath the top Acoustic Basement surface (cf. Howell et al. 2019). In the west, the  
572 granite displays a laccolith style geometry and extends up to ~3 s TWT (Figure 5). In the east, it  
573 displays a more domal geometry that extends up to ~5 s TWT, and stops at greater depths beneath the  
574 Acoustic Basement (Figure 6). Relief on the top surface of granitic bodies has also been identified in  
575 the Lake District and North Pennine batholiths onshore UK (Howell et al. 2019). We propose that the  
576 relief atop the granite and its depth beneath the top Acoustic Basement surface is expressed in the rift  
577 physiography, controlling the location of embayments along the footwall of the Terrane Boundary  
578 Fault (Figure 16). In areas where the granitic body extends to shallow depths beneath the top Acoustic  
579 Basement surface, we identify a steep shear zone with a series of fault blocks detaching along its  
580 margin (Figure 5, 16). However, where the granite sits at greater depths beneath the top Acoustic  
581 Basement surface, the upper part of the shear zone rotates to shallower dips across the top of the  
582 granite and incises backwards into the TBF Footwall Block, creating embayments that contain  
583 'perched' fault blocks atop a sub-horizontal detachment (Figure 6, 16). This indicates that the shallow  
584 relatively unfaulted areas of the TBF Footwall Block represent areas where the granite reaches  
585 shallow depths within basement and that the overall physiography of the TBF Footwall Block may act  
586 as a proxy for that of the underlying granite (Figure 4a, 16).

587 The granite-cored TBF Footwall Block is relatively unfaulted and forms a structural high relative to  
588 adjacent areas. Furthermore, the areas where the granite is located at shallow depths form further  
589 relative highs within the TBF Footwall Block (Figure 4). Granitic bodies often form the core to  
590 basement structural highs such as the Utsira High in the North Sea (Slagstad et al. 2011; Lundmark et  
591 al. 2013); the Alston Block in the UK (Critchley 1984; Howell et al. 2019) and the Sierra Nevada  
592 Batholith in the USA (Ducea & Saleeby 1996; Van Buer et al. 2009). Previous studies have proposed



593 that the reduced density and increased rigidity of granite compared to adjacent basement rocks makes  
594 them less susceptible to rifting when exposed to extensional stresses (Bott et al. 1958; de Castro et al.  
595 2007). Whilst this increased buoyancy plays an important role in the formation of granite-cored  
596 structural highs, isostatic forces relating to initial granite emplacement also play an important role  
597 (Howell et al. 2019). These granitic bodies show a partitioning of strain and deformation around their  
598 margins rather than internally. One potential mechanism for the lack of faulting across granite-cored  
599 structural highs may be the absence of prominent heterogeneities within these relatively homogeneous  
600 bodies upon which strain can initially localise (Mair & Green 1981; Howell et al. 2019).

### 601 **6.3 Strain accommodation along a laterally inhibited fault system**

602 The Splaying Fault System segments as it approaches the granite-cored TBF Footwall Block (Figure  
603 4). Cumulative fault throw remains relatively constant across the system as it approaches the block,  
604 with a large displacement gradient present at the boundary with the block itself (Figure 9, 10). The  
605 relatively constant cumulative throw along the fault indicates a large degree of kinematic coherence  
606 within the system, with individual fault segments behaving as a singular system (Walsh & Watterson  
607 1991; Walsh et al. 2002; Walsh et al. 2003; Childs et al. 2017; Jackson et al. 2017; Rotevatn et al.  
608 2018a). In cross-section, some faults also appear linked at depth, forming a single structure indicative  
609 of a degree of geometric coherence (Figure 8) (Walsh & Watterson 1991; Walsh et al. 2003; Giba et  
610 al. 2012; Jackson et al. 2017). However, the NW-dipping fault segments splaying from the footwall  
611 block of the main structure display kinematic coherence with the main system but are not  
612 geometrically linked (Figure 8).

613 Although a steep gradient is present for cumulative throw on the Splaying Fault System at the  
614 boundary with the TBF Footwall Block, such a gradient is not apparent for the individual segments  
615 themselves, which display more typical throw profiles (Figure 9, 10) (Childs et al. 2017). As the  
616 Splaying Fault System approaches this mechanically stronger barrier to lateral fault propagation, it  
617 splays into a series of lower displacement segments. These segments display lower throw gradients  
618 and are able to terminate easier than a single large structure (Figure 15b). Similar splaying fault

619 geometries are present at fault terminations across all scales. Deformation along the Alpine Fault is  
620 accommodated by splays of the Marlborough fault system to the northwest, where it starts to interact  
621 with the Hikurangi subduction zone (Norris & Cooper 2001; Wannamaker et al. 2009). The eastern  
622 branch of the East African Rift forms a series of rift segments to the south, termed the North Tanzania  
623 Divergence Zone, where strain is accommodated over a wider area as rifting propagates toward and  
624 eventually terminates in the cratonic lithosphere of the Tanzania Craton (Ebinger et al. 1997; Foster et  
625 al. 1997; Ring et al. 2005). At smaller scales, geometrically similar structures, such as horsetail splays  
626 and damage zones are commonly associated with the lateral terminations of fault systems (Kim &  
627 Sanderson 2006; Mouslopoulou et al. 2007; Perrin et al. 2016; Nicol et al. 2017).

628 A key question remains whether the fault propagated towards the footwall block or whether the  
629 system formed geologically instantaneously (i.e. following the constant length fault model) (Walsh et  
630 al. 2002; Childs et al. 2017; Nicol et al. 2017) but displayed different structural styles along its length.  
631 Furthermore, it is also unclear why the fault splayed at this particular location, outboard of the TBF  
632 Footwall Block, rather than at the boundary. Nixon et al. (2014) document a transition from localised  
633 to distributed extension within a kinematically coherent fault system in the Whakatane Graben, which  
634 they link to progressive strain localisation along the system. However, the segmentation in this  
635 instance occurs over a relatively short distance and does not resemble the gradual increase in  
636 segmentation, and the area over which strain is accommodated, observed in the Great South Basin  
637 (Figure 4, 15b). If the entire fault length did form geologically instantaneously, rather than propagate  
638 to the southwest, why the fault changed structural style in that specific location would still require an  
639 explanation, as the boundary with the TBF Footwall Block is located further to the southwest, with no  
640 major change in underlying structure at the point of initial splaying. Damage zones relating to granite  
641 emplacement may have locally altered lithological properties of basement rocks; however, this would  
642 only affect a limited area. In addition, local rotation and alignment of fault segments are only  
643 identified along the margin of the TBF Footwall Block (Figure 4, 11), and are not present where the  
644 fault begins to splay. Based on the gradational splaying of the fault system and the apparent lack of  
645 change in basement physiography at the initial site of segmentation, we suggest that the fault

646 propagated towards the granite block, although the timescale of this propagation is shorter than the  
647 temporal resolution provided by our seismic data.

648 As the faults rotate at the margin of the TBF Footwall Block, they appear to detach onto the granite  
649 (Figure 3, 8d), implying that the northern margin of the granite dips northwards. One possibility for  
650 why the fault splays where it does is that the dipping margin of the stronger granitic block restricts the  
651 maximum fault height, such that where the faults interact with the granite boundary at depth is offset  
652 from the boundary at the surface (Figure 15b). The initial site of fault splaying may correspond to the  
653 area where the deeper levels of the fault start to interact with the granite body. As the fault  
654 approaches, its maximum height is reduced, causing the fault to splay into multiple segments (Figure  
655 15b). This could potentially explain the splaying of the fault system, although we are unable to  
656 determine this scenario in our data.

657 As previously stated, individual fault segments rotate along the margin of the TBF Footwall Block  
658 (Figure 11, 15b). This may be related to local stress perturbations along the margin of the block  
659 (Morley 2010; Philippon et al. 2015; Morley 2017; Rotevatn et al. 2018b), or alternatively to a change  
660 in structural style along the faults from dip- to strike-slip (Mouslopoulou et al. 2007). The horsetail  
661 splay geometries identified across the intra-Upper Cretaceous surface (Figure 11) describe two  
662 WNW-trending grabens, which would not appear to fit with strike-slip motion. However, these  
663 grabens are not present at the top Acoustic Basement horizon and the individual faults may link  
664 together at depth, indicating that they could be related to oblique activity on a deeper fault. However,  
665 in other areas faults align along the margin of the TBF Footwall Block and show no evidence of  
666 strike-slip activity (Figure 4b). These faults appear to detach onto the north dipping northern margin  
667 of the granite, showing similar relationships to those along the Pakaha ridge (Figure 3, 8d). The  
668 rooting of faults onto the granitic body may also explain the switch in polarity along the Splaying  
669 Fault System, from SE-dipping in the northeast, to NW-dipping further southwest. In the southwest,  
670 the NW-dipping faults appear to detach onto the granite at depth, preferentially exploiting this pre-  
671 existing heterogeneity (Figure 8d).

672

673 **7. Conclusions**

674 In this study, we have analysed the detailed structural evolution of the southern section of the Great  
675 South Basin and examined how it has been influenced by various structural heterogeneities relating to  
676 the underlying Median Batholith Zone. We have documented a range of styles of structural  
677 inheritance, which exert variable influences over rift physiography throughout multiple tectonic  
678 events. We find that:

- 679 • The offshore extension of the terrane boundary between the Median Batholith Zone and  
680 Western Province terranes, trends WNW across the Great South Basin. This terrane boundary  
681 is associated with a crustal-to-lithospheric scale shear zone and is associated with a series of  
682 faults in the upper crust that segment the Great South Basin. Reactivation of the terrane  
683 boundary occurred in response to NE-SW oriented extension related to the separation of  
684 Australia and New Zealand.
- 685 • We postulate a granite cored structural high resides in the footwall of the reactivated terrane  
686 boundary. Based on seismic interpretation, regional context and nearby well information, we  
687 interpret that the granitic body displays a laccolith-style geometry and is part of the  
688 Cretaceous Separation Point Batholith suite. This batholith suite may have exploited the  
689 original lithosphere-scale terrane boundary along the southern margin of the Median Batholith  
690 and later appeared to localise the shear zone along its southern margin.
- 691 • We infer details of the 3D geometry of the granitic body from the overlying rift physiography.  
692 Where the granite reaches shallow depths, it controls the shallow geometry of the Terrane  
693 Boundary shear zone, which tracks along the granite margin and is associated with  
694 hangingwall fault blocks; where the granite top sits at greater depths, the shear zone shallows  
695 atop the granite and forms shallow embayments that incise into the footwall. These features  
696 act as a proxy for the relief of the top of the granite body.
- 697 • The granite-cored basement high acts as a barrier to the lateral propagation of NE-trending  
698 faults within the Median Batholith. These faults form a series of splays that eventually rotate

699 into parallelism as they approach the mechanically strong granite body, with relatively few  
700 faults present across the high itself. NE-trending faults formed in response to NW-SE directed  
701 extension related to the separation and breakup of New Zealand and West Antarctica.

- 702 • Individual segments within the splaying fault system display kinematic and geometric  
703 coherence along the fault system and accommodate similar values of extension along-strike.  
704 The initial site of splaying along the fault system is offset from the granite boundary, perhaps  
705 relating to a N-dipping granite margin.
- 706 • Two generations of basement fabrics are developed across the basin, trending E-W and NE-  
707 SW. These fabrics are proposed to be related to the reactivation of the terrane boundary and  
708 the NW-SE directed rifting respectively. They are exploited by numerous small, low-  
709 displacement faults, which are particularly well developed atop the granite-cored basement  
710 high.

711

## 712 **Acknowledgements**

713 This work is funded by the Leverhulme Trust in the form of a Leverhulme Early Career Fellowship  
714 awarded to Phillips. We would like to thank New Zealand Petroleum and Minerals for making the  
715 seismic data used in this study publically available. We would also like to thank Schlumberger for  
716 providing academic licences to the University of Durham for the use of Petrel software.

717

## 718 **Figure captions**

719 **Figure 1** – Map showing the top Acoustic Basement structure surface (in two way travel time – TWT)  
720 across the study area of the Great South Basin in relation to the underlying basement terranes. Terrane  
721 boundaries after Ghisetti (2010) and Mortimer et al. (2002). NE-trending faults are present throughout  
722 the basin, with a large WNW-trending fault present along its southern margin. Inset – regional map of  
723 New Zealand showing basement terranes offset along the Alpine Fault. Also shown are the locations

724 of the Great South and Canterbury basins offshore the South Island, as well as bathymetric features  
725 including the Campbell Plateau, Chatham Rise and Bounty Trough.

726 **Figure 2** – Stratigraphic column showing international and New Zealand stratigraphic ages for a  
727 series of prominent stratigraphic horizons and lithologies mapped throughout the basin. Stratigraphic  
728 horizons are tied to the Pukaki-1 well.

729 **Figure 3** – Uninterpreted and interpreted E-W oriented seismic section across the centre of the Great  
730 South Basin. See Figure 1 for location. Key stratigraphic horizons are linked to the Pakaha-1 well.  
731 Faults along the southwestern margin of the basin merge along the margin of the granitic Pakaha  
732 ridge. A complex series of cross-cutting faults are present in the centre of the basin.

733 **Figure 4** – A) TWT structure map of the top Acoustic Basement surface based on 3D seismic volume  
734 across the centre of the basin, see Figure 1 for location. The basin is dominated by NE-trending faults  
735 with the SSW-dipping Terrane Boundary Fault along the southern margin of the basin. A WNW-  
736 trending, relatively unfaulted structural high is located in the footwall of the Terrane Boundary Fault,  
737 termed the TBF Footwall Block. B) TWT structure map of a key surface within the Upper Cretaceous  
738 interval (see Figure 3). A SE-dipping fault becomes segmented towards the southwest and forms a  
739 series of splays as it approaches the TBF Footwall Block.

740 **Figure 5** – Uninterpreted and interpreted N-S oriented seismic section across the western platform of  
741 the study area. See Figure 1 for location. The boundary between the Median Batholith and Western  
742 Province terranes is marked by the blue line. Divergent syn-rift strata are marked by dark green  
743 wedges. A large shear zone is co-located with the boundary between the terranes.

744 **Figure 6** – uninterpreted and interpreted N-S oriented seismic section across the centre of the study  
745 area. See Figure 1 for location. Boundary between the Median Batholith and Western Province  
746 terranes is marked by the blue line and is associated with a shear zone and fault system, termed the  
747 Terrane Boundary Fault. A large area of complex faulting is present in the footwall of the Terrane  
748 Boundary Fault.

749 **Figure 7** – uninterpreted and interpreted N-S oriented seismic section across the TBF Footwall Block  
750 and a prominent footwall embayment. See Figure 4 for location. Basement reflectivity is shown  
751 associated with the Terrane Boundary Shear Zone and is cross-cut by fabrics associated with NE-  
752 trending faults.

753 **Figure 8** – Uninterpreted and interpreted seismic sections along-strike of the Splaying Fault System.  
754 See Figure 4 for locations. A) Section across the northeastern extent of the Splaying Fault System,  
755 where strain is accommodated by a single fault. Sub-Acoustic Basement reflectivity is present, likely  
756 relating to an earlier phase of activity of undetermined age. B) Towards the southwest the fault begins  
757 to splay into a series of segments. Synthetic fault segments form in response to dissection of the  
758 footwall as antithetic faults form in the hangingwall and merge with the main fault plane. C) The  
759 footwall of the fault is now highly deformed with extension accommodated by a wide zone of  
760 deformation consisting of SE- and NW-dipping faults. D) Extension is accommodated by a wide zone  
761 of deformation, with the dominant faults now dipping to the NW and detaching onto the margin of a  
762 granitic ridge. Rotation of the faults to a WNW-ESE strike is accommodated by the formation of  
763 shallow synthetic and antithetic faults in the footwall and hangingwall of the faults respectively.

764 **Figure 9** – Throw-length profiles calculated across the Acoustic Basement surface for individual  
765 segments of the Splaying Fault System. Individual profiles are colour-coded to the faults on the  
766 surface to the right. Also shown is the cumulative throw across the whole of the system, calculated by  
767 summing throw on individual segments across a lines perpendicular to the strike projection of the  
768 main fault. Also shown are the locations of the sections shown in Figure 8.

769 **Figure 10** – Throw-length profiles calculated across the intra-Upper Cretaceous surface for individual  
770 segments of the Splaying Fault System as well as the cumulative throw across the system. Fault  
771 colours are coded to the surface on the right, but are not related to those shown in Figure 9. Note that  
772 the cumulative throw is relatively consistent across the system regardless of the degree of  
773 segmentation, before a steep displacement gradient towards the boundary of the TBF Footwall Block.

774 **Figure 11** – Uninterpreted TWT structure map and detailed interpretations of horsetail-splay style  
775 fault geometries across the Intra-Upper Cretaceous surface. See Figure 4b for location. Fault numbers  
776 refer to those in Figure 10. Inset – Two seismic sections across the area corresponding to the blue and  
777 purple lines on the figure.

778 **Figure 12** – Uninterpreted and interpreted NNE-SSW oriented seismic sections across the TBF  
779 Footwall Block, highlighting the E-W oriented basement fabrics. See Figures 4 and 14 for location.  
780 Shear-zone related reflectivity is shown by the thick dashed black lines, whilst the basement fabrics  
781 are represented by the dark blue lines. NE-trending faults post-date and cross-cut the shear zone  
782 related reflectivity.

783 **Figure 13** – Uninterpreted and interpreted E-W oriented seismic section across the TBF Footwall  
784 Block, highlighting the NE-trending basement fabric. See Figures and 14 for location. The basement  
785 fabric displays a similar dip to the NE-trending faults and is often associated with low-displacement  
786 faults across the top Acoustic Basement surface.

787 **Figure 14** – TWT structure map showing E-W and NE-SW oriented faults associated with underlying  
788 fabrics across the top Acoustic Basement surface. See Figure 4a for location. Abutting and potentially  
789 cross-cutting relationships are observed between the different generations of faults, although no clear  
790 relative age relationships can be identified.

791 **Figure 15** – Schematic cartoons showing the different styles of structural inheritance identified in the  
792 Great South Basin across different scales. A) Shear zone and associated fault localise along the  
793 Terrane boundary and the margin of the continuation of the Separation Point Batholith Suite between  
794 the Median Batholith and Western Province. Inset shows the localisation of the shear zone along the  
795 granite margin. B) The stronger material in the footwall to the Terrane Boundary Fault forms a barrier  
796 to lateral fault propagation, causing faults to splay as they approach and strain to be accommodated  
797 across multiple low-displacement segments. Inset – The dipping boundary of the strong barrier  
798 restricts fault height away from the boundary at the surface, causing the initial site of fault splaying to  
799 be offset from the boundary at shallower depths. C) Exploitation of prominent basement fabrics by



800 relatively low-displacement faults. Differently oriented fabrics may be exploited at different times and  
801 during different tectonic events, resulting in multiple generations of faults. Inset – Cross-sectional  
802 view showing the reactivation and cross-cutting relationships between different fabrics.

803 **Figure 16** – 3D model showing the relationship between the Terrane Boundary Shear Zone and the  
804 relief of the top of the granitic body. The shear zone localises along the margin of the granite body.  
805 Where the granitic is situated at shallower depths the shear zone tracks along the margin and is  
806 associated with a series of detaching fault blocks; where the shear zone is situated at greater depths, it  
807 shallows atop the granite and forms embayments that cut back into the footwall.

808

809

## 810 **References**

811 Abdelmalak, M.M., Andersen, T.B., Planke, S., Faleide, J.I., Corfu, F., Tegner, C., Shephard, G.E.,  
812 Zastrozhnov, D., *et al.* 2015. The ocean-continent transition in the mid-Norwegian margin: Insight  
813 from seismic data and an onshore Caledonian field analogue. *Geology*, **43**, 1011-1014,  
814 <http://doi.org/10.1130/G37086.1>.

815  
816 Allibone, A.H. & Tulloch, A.J. 2004. Geology of the plutonic basement rocks of Stewart Island, New  
817 Zealand. *New Zealand Journal of Geology and Geophysics*, **47**, 233-256,  
818 <http://doi.org/10.1080/00288306.2004.9515051>.

819  
820 Allibone, A.H. & Tulloch, A.J. 2008. Early Cretaceous dextral transpressional deformation within the  
821 Median Batholith, Stewart Island, New Zealand. *New Zealand Journal of Geology and Geophysics*, **51**,  
822 115-134, <http://doi.org/10.1080/00288300809509854>.

823  
824 Bache, F., Sutherland, R., Stagpoole, V., Herzer, R., Collot, J. & Rouillard, P. 2012. Stratigraphy of the  
825 southern Norfolk Ridge and the Reinga Basin: A record of initiation of Tonga–Kermadec–Northland  
826 subduction in the southwest Pacific. *Earth and Planetary Science Letters*, **321-322**, 41-53,  
827 <http://doi.org/https://doi.org/10.1016/j.epsl.2011.12.041>.

828  
829 Bache, F., Mortimer, N., Sutherland, R., Collot, J., Rouillard, P., Stagpoole, V. & Nicol, A. 2014. Seismic  
830 stratigraphic record of transition from Mesozoic subduction to continental breakup in the Zealandia  
831 sector of eastern Gondwana. *Gondwana Research*, **26**, 1060-1078,  
832 <http://doi.org/https://doi.org/10.1016/j.gr.2013.08.012>.

833

834 Beggs, J. 1993. Depositional and tectonic history of the Great South Basin. *South Pacific sedimentary*  
835 *basins. Sedimentary basins of the World*, **2**, 365-373.

836

837 Bishop, D., Bradshaw, J. & Landis, C. 1985. Provisional terrane map of South Island, New Zealand.

838

839 Bott, M.H.P., Day, A.A. & Masson-Smith, D. 1958. The Geological Interpretation of Gravity and  
840 Magnetic Surveys in Devon and Cornwall. *Philosophical Transactions of the Royal Society of London*  
841 *Series a-Mathematical and Physical Sciences*, **251**, 161-191, <http://doi.org/10.1098/rsta.1958.0013>.

842

843 Bradshaw, J.D. 1989. Cretaceous Geotectonic Patterns in the New-Zealand Region. *Tectonics*, **8**, 803-  
844 820, <http://doi.org/10.1029/TC008i004p00803>.

845

846 Campbell, H.J., Mortimer, N. & Turnbull, I.M. 2003. Murihiku Supergroup, New Zealand: Redefined.  
847 *Journal of the Royal Society of New Zealand*, **33**, 85-95,  
848 <http://doi.org/10.1080/03014223.2003.9517722>.

849

850 Carreras, J. 2001. Zooming on Northern Cap de Creus shear zones. *Journal of Structural Geology*, **23**,  
851 1457-1486, [http://doi.org/https://doi.org/10.1016/S0191-8141\(01\)00011-6](http://doi.org/https://doi.org/10.1016/S0191-8141(01)00011-6).

852

853 Chattopadhyay, A. & Chakra, M. 2013. Influence of pre-existing pervasive fabrics on fault patterns  
854 during orthogonal and oblique rifting: An experimental approach. *Marine and Petroleum Geology*,  
855 **39**, 74-91, <http://doi.org/http://dx.doi.org/10.1016/j.marpetgeo.2012.09.009>.

856

857 Childs, C., Holdsworth, R.E., Jackson, C.A.L., Manzocchi, T., Walsh, J.J. & Yielding, G. 2017.  
858 Introduction to the geometry and growth of normal faults. *Geological Society, London, Special*  
859 *Publications*, **439**, 1, <http://doi.org/10.1144/SP439.24>.

860

861 Coleman, A.J., Jackson, C.A.L., Nikolinakou, M.A. & Duffy, O.B. 2018. How, where, and when do radial  
862 faults grow near salt diapirs? *Geology*, **46**, 655-658, <http://doi.org/10.1130/G40338.1>.

863

864 Collanega, L., Jackson, C.A.L., Bell, R.E., Coleman, A.J., Lenhart, A. & Breda, A. 2018. Normal fault  
865 growth influenced by basement fabrics: the importance of preferential nucleation from pre-existing  
866 structures. *Basin Research*, **0**, <http://doi.org/10.1111/bre.12327>.

867

868 Cooper, A.F. & Norris, R.J. 1994. Anatomy, structural evolution, and slip rate of a plate-boundary  
869 thrust: The Alpine fault at Gaunt Creek, Westland, New Zealand. *GSA Bulletin*, **106**, 627-633,  
870 [http://doi.org/10.1130/0016-7606\(1994\)106<0627:ASEASR>2.3.CO;2](http://doi.org/10.1130/0016-7606(1994)106<0627:ASEASR>2.3.CO;2).

871

872 Cooper, A.F., Barreiro, B.A., Kimbrough, D.L. & Mattinson, J.M. 1987. Lamprophyre dike intrusion  
873 and the age of the Alpine fault, New Zealand. *Geology*, **15**, 941-944, [http://doi.org/10.1130/0091-7613\(1987\)15<941:LDIATA>2.0.CO;2](http://doi.org/10.1130/0091-7613(1987)15<941:LDIATA>2.0.CO;2).

874

875

876 Corti, G. 2008. Control of rift obliquity on the evolution and segmentation of the main Ethiopian rift.  
877 *Nature Geoscience*, **1**, 258, <http://doi.org/10.1038/ngeo160>

878 <https://www.nature.com/articles/ngeo160#supplementary-information>.

879

880 Critchley, M.F. 1984. Variscan tectonics of the Alston block, northern England. *Geological Society,*

881 *London, Special Publications*, **14**, 139, <http://doi.org/10.1144/GSL.SP.1984.014.01.14>.

882

883 Daly, M.C., Chorowicz, J. & Fairhead, J.D. 1989. Rift basin evolution in Africa: the influence of

884 reactivated steep basement shear zones. *Geological Society, London, Special Publications*, **44**, 309,

885 <http://doi.org/10.1144/GSL.SP.1989.044.01.17>.

886

887 Davy, B., Hoernle, K. & Werner, R. 2008. Hikurangi Plateau: Crustal structure, rifted formation, and

888 Gondwana subduction history. *Geochemistry, Geophysics, Geosystems*, **9**,

889 <http://doi.org/10.1029/2007GC001855>.

890

891 Dawson, S.M., Laó-Dávila, D.A., Atekwana, E.A. & Abdelsalam, M.G. 2018. The influence of the

892 Precambrian Mughese Shear Zone structures on strain accommodation in the northern Malawi Rift.

893 *Tectonophysics*, **722**, 53-68, <http://doi.org/https://doi.org/10.1016/j.tecto.2017.10.010>.

894

895 de Castro, D.L., de Oliveira, D.C. & Gomes Castelo Branco, R.M. 2007. On the tectonics of the

896 Neocomian Rio do Peixe Rift Basin, NE Brazil: Lessons from gravity, magnetics, and radiometric data.

897 *Journal of South American Earth Sciences*, **24**, 184-202,

898 <http://doi.org/https://doi.org/10.1016/j.jsames.2007.04.001>.

899

900 De Paola, N., Holdsworth, R.E. & McCaffrey, K.J.W. 2005. The influence of lithology and pre-existing

901 structures on reservoir-scale faulting patterns in transtensional rift zones. *Journal of the Geological*

902 *Society*, **162**, 471, <http://doi.org/10.1144/0016-764904-043>.

903

904 Dichiarante, A.M., Holdsworth, R.E., Dempsey, E.D., Selby, D., McCaffrey, K.J.W., Michie, U.M.,

905 Morgan, G. & Bonniface, J. 2016. New structural and Re–Os geochronological evidence constraining

906 the age of faulting and associated mineralization in the Devonian Orcadian Basin, Scotland. *Journal*

907 *of the Geological Society*, **173**, 457, <http://doi.org/10.1144/jgs2015-118>.

908

909 Dore, A.G., Lundin, E.R., Fichler, C. & Olesen, O. 1997. Patterns of basement structure and

910 reactivation along the NE Atlantic margin. *Journal of the Geological Society*, **154**, 85-92,

911 [http://doi.org/DOI 10.1144/gsjgs.154.1.0085](http://doi.org/DOI%2010.1144/gsjgs.154.1.0085).

912

913 Ducea, M.N. & Saleeby, J.B. 1996. Buoyancy sources for a large, unrooted mountain range, the Sierra

914 Nevada, California: Evidence from xenolith thermobarometry. *Journal of Geophysical Research-Solid*

915 *Earth*, **101**, 8229-8244, <http://doi.org/10.1029/95jb03452>.

916

917 Duffy, O.B., Bell, R.E., Jackson, C.A.L., Gawthorpe, R.L. & Whipp, P.S. 2015. Fault growth and

918 interactions in a multiphase rift fault network: Horda Platform, Norwegian North Sea. *Journal of*

919 *Structural Geology*, **80**, 99-119, <http://doi.org/http://dx.doi.org/10.1016/j.jsg.2015.08.015>.

920

921 Ebinger, C., Djomani, Y.P., Mbede, E., Foster, A. & Dawson, J.B. 1997. Rifting Archaean lithosphere:  
922 the Eyasi-Manyara-Natron rifts, East Africa. *Journal of the Geological Society*, **154**, 947,  
923 <http://doi.org/10.1144/gsjgs.154.6.0947>.

924

925 Evans, D.J., Rowley, W.J., Chadwick, R.A. & Millward, D. 1993. Seismic reflections from within the  
926 Lake District batholith, Cumbria, northern England. *Journal of the Geological Society*, **150**, 1043,  
927 <http://doi.org/10.1144/gsjgs.150.6.1043>.

928

929 Evans, D.J., Rowley, W.J., Chadwick, R.A., Kimbell, G.S. & Millward, D. 1994. Seismic reflection data  
930 and the internal structure of the Lake District batholith, Cumbria, northern England. *Proceedings of*  
931 *the Yorkshire Geological and Polytechnic Society*, **50**, 11, <http://doi.org/10.1144/pygs.50.1.11>.

932

933 Fazlikhani, H., Fossen, H., Gawthorpe, R., Faleide, J.I. & Bell, R.E. 2017. Basement structure and its  
934 influence on the structural configuration of the northern North Sea rift. *Tectonics*, **36**, 1151-1177,  
935 <http://doi.org/10.1002/2017tc004514>.

936

937 Fossen, H., Khani, H.F., Faleide, J.I., Ksienzyk, A.K. & Dunlap, W.J. 2016. Post-Caledonian extension in  
938 the West Norway–northern North Sea region: the role of structural inheritance. *Geological Society,*  
939 *London, Special Publications*, **439**, <http://doi.org/https://doi.org/10.1144/SP439.6>.

940

941 Foster, A., Ebinger, C., Mbede, E. & Rex, D. 1997. Tectonic development of the northern Tanzanian  
942 sector of the East African Rift System. *Journal of the Geological Society*, **154**, 689,  
943 <http://doi.org/10.1144/gsjgs.154.4.0689>.

944

945 Freeman, B., Klemperer, S.L. & Hobbs, R.W. 1988. The deep structure of northern England and the  
946 Iapetus Suture zone from BIRPS deep seismic reflection profiles. *Journal of the Geological Society*,  
947 **145**, 727, <http://doi.org/10.1144/gsjgs.145.5.0727>.

948

949 Ghisetti, F. 2010. Seismic interpretation, Prospects and Structural Analysis, Great South Basin.  
950 Ministry of Economic Development New Zealand Unpublished Petroleum Report PR4173.

951

952 Giba, M., Walsh, J.J. & Nicol, A. 2012. Segmentation and growth of an obliquely reactivated normal  
953 fault. *Journal of Structural Geology*, **39**, 253-267, <http://doi.org/10.1016/j.jsg.2012.01.004>.

954

955 Grobys, J.W.G., Gohl, K., Uenzelmann-Neben, G., Davy, B. & Barker, D. 2009. Extensional and  
956 magmatic nature of the Campbell Plateau and Great South Basin from deep crustal studies.  
957 *Tectonophysics*, **472**, 213-225, <http://doi.org/https://doi.org/10.1016/j.tecto.2008.05.003>.

958

959 Grobys, J.W.G., Gohl, K., Davy, B., Uenzelmann-Neben, G., Deen, T. & Barker, D. 2007. Is the Bounty  
960 Trough off eastern New Zealand an aborted rift? *Journal of Geophysical Research: Solid Earth*, **112**,  
961 <http://doi.org/10.1029/2005JB004229>.

962

963 Hedin, P., Almqvist, B., Berthet, T., Juhlin, C., Buske, S., Simon, H., Giese, R., Krauß, F., *et al.* 2016. 3D  
964 reflection seismic imaging at the 2.5km deep COSC-1 scientific borehole, central Scandinavian

965 Caledonides. *Tectonophysics*, **689**, 40-55,  
966 <http://doi.org/https://doi.org/10.1016/j.tecto.2015.12.013>.

967  
968 Heilman, E., Kolawole, F., Atekwana, E.A. & Mayle, M. 2019. Controls of Basement Fabric on the  
969 Linkage of Rift Segments. *Tectonics*, **0**, <http://doi.org/10.1029/2018TC005362>.

970  
971 Henstra, G.A., Rotevatn, A., Gawthorpe, R.L. & Ravnås, R. 2015. Evolution of a major segmented  
972 normal fault during multiphase rifting: The origin of plan-view zigzag geometry. *Journal of Structural*  
973 *Geology*, **74**, 45-63, <http://doi.org/https://doi.org/10.1016/j.jsg.2015.02.005>.

974  
975 Heron, P.J., Peace, A.L., McCaffrey, K., Welford, J.K., Wilson, R., van Hunen, J. & Pysklywec, R.N.  
976 2019. Segmentation of rifts through structural inheritance: Creation of the Davis Strait. *Tectonics*, **0**,  
977 <http://doi.org/10.1029/2019TC005578>.

978  
979 Higgs, K.E., Browne, G.H. & Sahoo, T.R. 2019. Reservoir characterisation of syn-rift and post-rift  
980 sandstones in frontier basins: An example from the Cretaceous of Canterbury and Great South  
981 basins, New Zealand. *Marine and Petroleum Geology*, **101**, 1-29,  
982 <http://doi.org/https://doi.org/10.1016/j.marpetgeo.2018.11.030>.

983  
984 Howell, D.G. 1980. Mesozoic accretion of exotic terranes along the New Zealand segment of  
985 Gondwanaland. *Geology*, **8**, 487-491, [http://doi.org/10.1130/0091-  
986 7613\(1980\)8<487:MAOETA>2.0.CO;2](http://doi.org/10.1130/0091-7613(1980)8<487:MAOETA>2.0.CO;2).

987  
988 Howell, L., Egan, S., Leslie, G. & Clarke, S. 2019. Structural and geodynamic modelling of the  
989 influence of granite bodies during lithospheric extension: Application to the Carboniferous basins of  
990 northern England. *Tectonophysics*, <http://doi.org/https://doi.org/10.1016/j.tecto.2019.02.008>.

991  
992 Jackson, C.A.L., Bell, R.E., Rotevatn, A. & Tvedt, A.B.M. 2017. Techniques to determine the  
993 kinematics of synsedimentary normal faults and implications for fault growth models. *Geological*  
994 *Society, London, Special Publications*, **439**, SP439.422, <http://doi.org/10.1144/SP439.22>.

995  
996 Johnston, M.R. 2019. Chapter 2 The path to understanding the central terranes of Zealandia.  
997 *Geological Society, London, Memoirs*, **49**, 15-30, <http://doi.org/10.1144/m49.2>.

998  
999 Jones, T.D. & Nur, A. 1984. The nature of seismic reflections from deep crustal fault zones. *Journal of*  
1000 *Geophysical Research: Solid Earth*, **89**, 3153-3171, <http://doi.org/10.1029/JB089iB05p03153>.

1001  
1002 Jongens, R. 2006. Structure of the Buller and Takaka Terrane rocks adjacent to the Anatoki Fault,  
1003 northwest Nelson, New Zealand. *New Zealand Journal of Geology and Geophysics*, **49**, 443-461,  
1004 <http://doi.org/10.1080/00288306.2006.9515180>.

1005  
1006 Kim, Y.-S. & Sanderson, D.J. 2006. Structural similarity and variety at the tips in a wide range of  
1007 strike-slip faults: a review. *Terra Nova*, **18**, 330-344, [http://doi.org/10.1111/j.1365-  
1008 3121.2006.00697.x](http://doi.org/10.1111/j.1365-3121.2006.00697.x).

1009  
1010 Kirkpatrick, J.D., Bezerra, F.H.R., Shipton, Z.K., Do Nascimento, A.F., Pytharouli, S.I., Lunn, R.J. &  
1011 Soden, A.M. 2013. Scale-dependent influence of pre-existing basement shear zones on rift faulting: a  
1012 case study from NE Brazil. *Journal of the Geological Society*, **170**, 237,  
1013 <http://doi.org/10.1144/jgs2012-043>.

1014  
1015 Koopmann, H., Brune, S., Franke, D. & Breuer, S. 2014. Linking rift propagation barriers to excess  
1016 magmatism at volcanic rifted margins. *Geology*, **42**, 1071-1074, <http://doi.org/10.1130/G36085.1>.

1017  
1018 Kula, J., Tulloch, A., Spell, T.L. & Wells, M.L. 2007. Two-stage rifting of Zealandia-Australia-Antarctica:  
1019 Evidence from <sup>40</sup>Ar/<sup>39</sup>Ar thermochronometry of the Sisters shear zone, Stewart Island, New  
1020 Zealand. *Geology*, **35**, 411-414, <http://doi.org/10.1130/g23432a.1>.

1021  
1022 Kula, J., Tulloch, A.J., Spell, T.L., Wells, M.L. & Zanetti, K.A. 2009. Thermal evolution of the Sisters  
1023 shear zone, southern New Zealand; Formation of the Great South Basin and onset of Pacific-  
1024 Antarctic spreading. *Tectonics*, **28**, <http://doi.org/10.1029/2008TC002368>.

1025  
1026 Landis, C.A., Campbell, H.J., Aslund, T., Cawood, P.A., Douglas, A., Kimbrough, D.L., Pillai, D.D.L.,  
1027 Raine, J.I., *et al.* 1999. Permian-Jurassic strata at Productus Creek, Southland, New Zealand:  
1028 Implications for terrane dynamics of the eastern Gondwanaland margin. *New Zealand Journal of*  
1029 *Geology and Geophysics*, **42**, 255-278, <http://doi.org/10.1080/00288306.1999.9514844>.

1030  
1031 Lenhart, A., Jackson, C.A.L., Bell, R.E., Duffy, O.B., Gawthorpe, R.L. & Fossen, H. 2019. Structural  
1032 architecture and composition of crystalline basement offshore west Norway.  
1033 <http://doi.org/10.1130/L668.1>.

1034  
1035 Long, J.J. & Imber, J. 2012. Strain compatibility and fault linkage in relay zones on normal faults.  
1036 *Journal of Structural Geology*, **36**, 16-26, <http://doi.org/https://doi.org/10.1016/j.jsg.2011.12.013>.

1037  
1038 Lundmark, A.M., Saether, T. & Sorlie, R. 2013. Ordovician to Silurian magmatism on the Utsira High,  
1039 North Sea: implications for correlations between the onshore and offshore Caledonides. *Geological*  
1040 *Society, London, Special Publications*, **390**, 513-523, <http://doi.org/10.1144/sp390.21>.

1041  
1042 Lynn, H.B., Hale, L.D. & Thompson, G.A. 1981. Seismic Reflections from the Basal Contacts of  
1043 Batholiths. *Journal of Geophysical Research*, **86**, 633-638, <http://doi.org/10.1029/JB086iB11p10633>.

1044  
1045 Magee, C., McDermott, K.G., Stevenson, C.T.E. & Jackson, C.A.L. 2014. Influence of crystallised  
1046 igneous intrusions on fault nucleation and reactivation during continental extension. *Journal of*  
1047 *Structural Geology*, **62**, 183-193, <http://doi.org/https://doi.org/10.1016/j.jsg.2014.02.003>.

1048  
1049 Mair, J.A. & Green, A.G. 1981. High-resolution seismic reflection profiles reveal fracture zones within  
1050 a 'homogeneous' granite batholith. *Nature*, **294**, 439-442, <http://doi.org/10.1038/294439a0>.

1051  
1052 McCaffrey, K.J.W. & Petford, N. 1997. Are granitic intrusions scale invariant? *Journal of the*  
1053 *Geological Society*, **154**, 1, <http://doi.org/10.1144/gsjgs.154.1.0001>.

1054  
1055 McLean, C.E., Schofield, N., Brown, D.J., Jolley, D.W. & Reid, A. 2017. 3D seismic imaging of the  
1056 shallow plumbing system beneath the Ben Nevis Monogenetic Volcanic Field: Faroe–Shetland Basin.  
1057 *Journal of the Geological Society*, **174**, 468, <http://doi.org/10.1144/jgs2016-118>.

1058  
1059 McWilliams, M.O. & Howell, D.G. 1982. Exotic terranes of western California. *Nature*, **297**, 215-217,  
1060 <http://doi.org/10.1038/297215a0>.

1061  
1062 Morley, C.K. 2010. Stress re-orientation along zones of weak fabrics in rifts: An explanation for pure  
1063 extension in 'oblique' rift segments? *Earth and Planetary Science Letters*, **297**, 667-673,  
1064 <http://doi.org/https://doi.org/10.1016/j.epsl.2010.07.022>.

1065  
1066 Morley, C.K. 2017. The impact of multiple extension events, stress rotation and inherited fabrics on  
1067 normal fault geometries and evolution in the Cenozoic rift basins of Thailand. *Geological Society,  
1068 London, Special Publications*, **439**, 413, <http://doi.org/10.1144/SP439.3>.

1069  
1070 Morley, C.K., Haranya, C., Phoosongsee, W., Pongwapee, S., Kornsawan, A. & Wonganan, N. 2004.  
1071 Activation of rift oblique and rift parallel pre-existing fabrics during extension and their effect on  
1072 deformation style: examples from the rifts of Thailand. *Journal of Structural Geology*, **26**, 1803-1829,  
1073 <http://doi.org/https://doi.org/10.1016/j.jsg.2004.02.014>.

1074  
1075 Morley, C.K., Maczak, A., Rungprom, T., Ghosh, J., Cartwright, J.A., Bertoni, C. & Panpichityota, N.  
1076 2017. New style of honeycomb structures revealed on 3D seismic data indicate widespread  
1077 diagenesis offshore Great South Basin, New Zealand. *Marine and Petroleum Geology*, **86**, 140-154,  
1078 <http://doi.org/10.1016/j.marpetgeo.2017.05.035>.

1079  
1080 Mortimer, E.J., Paton, D.A., Scholz, C.A. & Strecker, M.R. 2016. Implications of structural inheritance  
1081 in oblique rift zones for basin compartmentalization: Nkhata Basin, Malawi Rift (EARS). *Marine and  
1082 Petroleum Geology*, **72**, 110-121, <http://doi.org/https://doi.org/10.1016/j.marpetgeo.2015.12.018>.

1083  
1084 Mortimer, N. 2004. New Zealand's Geological Foundations. *Gondwana Research*, **7**, 261-272,  
1085 [http://doi.org/https://doi.org/10.1016/S1342-937X\(05\)70324-5](http://doi.org/https://doi.org/10.1016/S1342-937X(05)70324-5).

1086  
1087 Mortimer, N. 2014. The oroclinal bend in the South Island, New Zealand. *Journal of Structural  
1088 Geology*, **64**, 32-38, <http://doi.org/https://doi.org/10.1016/j.jsg.2013.08.011>.

1089  
1090 Mortimer, N., Tulloch, A.J. & Ireland, T.R. 1997. Basement geology of Taranaki and Wanganui Basins,  
1091 New Zealand. *New Zealand Journal of Geology and Geophysics*, **40**, 223-236,  
1092 <http://doi.org/10.1080/00288306.1997.9514754>.

1093  
1094 Mortimer, N., Davey, F.J., Melhuish, A., Yu, J. & Godfrey, N.J. 2002. Geological interpretation of a  
1095 deep seismic reflection profile across the Eastern Province and Median Batholith, New Zealand:  
1096 Crustal architecture of an extended Phanerozoic convergent orogen. *New Zealand Journal of  
1097 Geology and Geophysics*, **45**, 349-363, <http://doi.org/10.1080/00288306.2002.9514978>.

1098

1099 Mortimer, N., Tulloch, A.J., Spark, R.N., Walker, N.W., Ladley, E., Allibone, A. & Kimbrough, D.L. 1999.  
1100 Overview of the Median Batholith, New Zealand: a new interpretation of the geology of the Median  
1101 Tectonic Zone and adjacent rocks. *Journal of African Earth Sciences*, **29**, 257-268,  
1102 [http://doi.org/https://doi.org/10.1016/S0899-5362\(99\)00095-0](http://doi.org/https://doi.org/10.1016/S0899-5362(99)00095-0).

1103  
1104 Mouslopoulou, V., Nicol, A., Little, T.A. & Walsh, J.J. 2007. Displacement transfer between  
1105 intersecting regional strike-slip and extensional fault systems. *Journal of Structural Geology*, **29**, 100-  
1106 116, <http://doi.org/https://doi.org/10.1016/j.jsg.2006.08.002>.

1107  
1108 Muir, R.J., Bradshaw, J.D., Weaver, S.D. & Laird, M.G. 2000. The influence of basement structure on  
1109 the evolution of the Taranaki Basin, New Zealand. *Journal of the Geological Society*, **157**, 1179,  
1110 <http://doi.org/10.1144/jgs.157.6.1179>.

1111  
1112 Nicol, A., Childs, C., Walsh, J.J., Manocchi, T. & Schöpfer, M.P.J. 2017. Interactions and growth of  
1113 faults in an outcrop-scale system. *Geological Society, London, Special Publications*, **439**, 23,  
1114 <http://doi.org/10.1144/SP439.9>.

1115  
1116 Nixon, C.W., Bull, J.M. & Sanderson, D.J. 2014. Localized vs distributed deformation associated with  
1117 the linkage history of an active normal fault, Whakatane Graben, New Zealand. *Journal of Structural*  
1118 *Geology*, **69**, 266-280, <http://doi.org/https://doi.org/10.1016/j.jsg.2014.06.005>.

1119  
1120 Norris, R.J. & Cooper, A.F. 2001. Late Quaternary slip rates and slip partitioning on the Alpine Fault,  
1121 New Zealand. *Journal of Structural Geology*, **23**, 507-520,  
1122 [http://doi.org/https://doi.org/10.1016/S0191-8141\(00\)00122-X](http://doi.org/https://doi.org/10.1016/S0191-8141(00)00122-X).

1123  
1124 Paton, D.A. & Underhill, J.R. 2004. Role of crustal anisotropy in modifying the structural and  
1125 sedimentological evolution of extensional basins: the Gamtoos Basin, South Africa. *Basin Research*,  
1126 **16**, 339-359, <http://doi.org/10.1111/j.1365-2117.2004.00237.x>.

1127  
1128 Paton, D.A., Mortimer, E.J., Hodgson, N. & van der Spuy, D. 2016. The missing piece of the South  
1129 Atlantic jigsaw: when continental break-up ignores crustal heterogeneity. *Geological Society,*  
1130 *London, Special Publications*, **438**, SP438.438, <http://doi.org/10.1144/SP438.8>.

1131  
1132 Peace, A., McCaffrey, K., Imber, J., van Hunen, J., Hobbs, R. & Wilson, R. 2017. The role of pre-  
1133 existing structures during rifting, continental breakup and transform system development, offshore  
1134 West Greenland. *Basin Research*, 373-394, <http://doi.org/https://doi.org/10.1111/bre.12257>.

1135  
1136 Perrin, C., Manighetti, I. & Gaudemer, Y. 2016. Off-fault tip splay networks: A genetic and generic  
1137 property of faults indicative of their long-term propagation. *Comptes Rendus Geoscience*, **348**, 52-60,  
1138 <http://doi.org/https://doi.org/10.1016/j.crte.2015.05.002>.

1139  
1140 Petford, N. & Atherton, M.P. 1992. Granitoid emplacement and deformation along a major crustal  
1141 lineament: The Cordillera Blanca, Peru. *Tectonophysics*, **205**, 171-185,  
1142 [http://doi.org/https://doi.org/10.1016/0040-1951\(92\)90425-6](http://doi.org/https://doi.org/10.1016/0040-1951(92)90425-6).

1143



1144 Petford, N., Cruden, A.R., McCaffrey, K.J.W. & Vigneresse, J.L. 2000. Granite magma formation,  
1145 transport and emplacement in the Earth's crust. *Nature*, **408**, 669-673,  
1146 <http://doi.org/10.1038/35047000>.

1147  
1148 Philippon, M., Willingshofer, E., Sokoutis, D., Corti, G., Sani, F., Bonini, M. & Cloetingh, S. 2015. Slip  
1149 re-orientation in oblique rifts. *Geology*, **43**, 147-150, <http://doi.org/10.1130/G36208.1>.

1150  
1151 Phillips, T.B., Magee, C., Jackson, C.A.L. & Bell, R.E. 2017. Determining the three-dimensional  
1152 geometry of a dike swarm and its impact on later rift geometry using seismic reflection data.  
1153 *Geology*, **46**, 119-122, <http://doi.org/10.1130/G39672.1>.

1154  
1155 Phillips, T.B., Jackson, C.A.L., Bell, R.E. & Duffy, O.B. 2018. Oblique reactivation of lithosphere-scale  
1156 lineaments controls rift physiography – the upper-crustal expression of the Sorgenfrei–Tornquist  
1157 Zone, offshore southern Norway. *Solid Earth*, **9**, 403-429, <http://doi.org/10.5194/se-9-403-2018>.

1158  
1159 Phillips, T.B., Jackson, C.A., Bell, R.E., Duffy, O.B. & Fossen, H. 2016. Reactivation of intrabasement  
1160 structures during rifting: A case study from offshore southern Norway. *Journal of Structural Geology*,  
1161 **91**, 54-73, <http://doi.org/10.1016/j.jsg.2016.08.008>.

1162  
1163 Reeve, M.T., Bell, R.E. & Jackson, C.A.L. 2013. Origin and significance of intra-basement seismic  
1164 reflections offshore western Norway. *Journal of the Geological Society*, **171**, 1-4,  
1165 <http://doi.org/10.1144/jgs2013-020>.

1166  
1167 Rennie, S.F., Fagereng, Å. & Diener, J.F.A. 2013. Strain distribution within a km-scale, mid-crustal  
1168 shear zone: The Kuckaus Mylonite Zone, Namibia. *Journal of Structural Geology*, **56**, 57-69,  
1169 <http://doi.org/https://doi.org/10.1016/j.jsg.2013.09.001>.

1170  
1171 Ring, U.W.E., Schwartz, H.L., Bromage, T.G. & Sanaane, C. 2005. Kinematic and sedimentological  
1172 evolution of the Manyara Rift in northern Tanzania, East Africa. *Geological Magazine*, **142**, 355-368,  
1173 <http://doi.org/10.1017/S0016756805000841>.

1174  
1175 Robertson, A.H.F. & Palamakumbura, R. 2019. Chapter 9 Sedimentary development of the Mid-  
1176 Permian–Mid-Triassic Maitai continental margin forearc basin, South Island, New Zealand.  
1177 *Geological Society, London, Memoirs*, **49**, 189-230, <http://doi.org/10.1144/m49.9>.

1178  
1179 Robertson, A.H.F., Campbell, H.J., Johnston, M.R. & Palamakumbura, R. 2019. Chapter 15  
1180 Construction of a Paleozoic–Mesozoic accretionary orogen along the active continental margin of SE  
1181 Gondwana (South Island, New Zealand): summary and overview. *Geological Society, London,*  
1182 *Memoirs*, **49**, 331-372, <http://doi.org/10.1144/m49.8>.

1183  
1184 Rotevatn, A., Jackson, C.A.L., Tvedt, A.B.M., Bell, R.E. & Blækkam, I. 2018a. How do normal faults  
1185 grow? *Journal of Structural Geology*, <http://doi.org/https://doi.org/10.1016/j.jsg.2018.08.005>.

1186  
1187 Rotevatn, A., Kristensen, T.B., Ksienzyk, A.K., Wemmer, K., Henstra, G.A., Midtkandal, I., Grundvåg,  
1188 S.-A. & Andresen, A. 2018b. Structural Inheritance and Rapid Rift-Length Establishment in a

1189 Multiphase Rift: The East Greenland Rift System and its Caledonian Orogenic Ancestry. *Tectonics*, **37**,  
1190 1858-1875, <http://doi.org/doi:10.1029/2018TC005018>.

1191

1192 Sahoo, T., King, P., Bland, K., Strogon, D., Sykes, R. & Bache, F. 2014. Tectono-sedimentary evolution  
1193 and source rock distribution of the mid to Late Cretaceous succession in the Great South Basin, New  
1194 Zealand *The APPEA Journal*, **54**, 259-274, <http://doi.org/https://doi.org/10.1071/AJ13026>.

1195

1196 Samsu, A., Cruden, A.R., Hall, M., Micklethwaite, S. & Denyszyn, S.W. 2019. The influence of  
1197 basement faults on local extension directions: Insights from potential field geophysics and field  
1198 observations. *Basin Research*, **0**, <http://doi.org/10.1111/bre.12344>.

1199

1200 Schwartz, J.J., Johnson, K., Mueller, P., Strickland, A., Valley, J. & Wooden, J.L. 2014. Time scales and  
1201 processes of Cordilleran batholith construction and high-Sr/Y magmatic pulses: Evidence from the  
1202 Bald Mountain batholith, northeastern Oregon. *Geosphere*, **10**, 1456-1481,  
1203 <http://doi.org/10.1130/GES01033.1>.

1204

1205 Slagstad, T., Davidsen, B. & Daly, J.S. 2011. Age and composition of crystalline basement rocks on the  
1206 Norwegian continental margin: offshore extension and continuity of the Caledonian–Appalachian  
1207 orogenic belt. *Journal of the Geological Society*, **168**, 1167, [http://doi.org/10.1144/0016-76492010-](http://doi.org/10.1144/0016-76492010-136)  
1208 [136](http://doi.org/10.1144/0016-76492010-136).

1209

1210 Sutherland, R., Davey, F. & Beavan, J. 2000. Plate boundary deformation in South Island, New  
1211 Zealand, is related to inherited lithospheric structure. *Earth and Planetary Science Letters*, **177**, 141-  
1212 151, [http://doi.org/https://doi.org/10.1016/S0012-821X\(00\)00043-1](http://doi.org/https://doi.org/10.1016/S0012-821X(00)00043-1).

1213

1214 Sutherland, R., Collot, J., Lafoy, Y., Logan, G.A., Hackney, R., Stagpoole, V., Uruski, C., Hashimoto, T.,  
1215 *et al.* 2010. Lithosphere delamination with foundering of lower crust and mantle caused permanent  
1216 subsidence of New Caledonia Trough and transient uplift of Lord Howe Rise during Eocene and  
1217 Oligocene initiation of Tonga-Kermadec subduction, western Pacific. *Tectonics*, **29**,  
1218 <http://doi.org/10.1029/2009TC002476>.

1219

1220 Thomas, W.A. 2006. Tectonic inheritance at a continental margin. *GSA Today*, **16**, 4-11,  
1221 [http://doi.org/10.1130/1052-5173\(2006\)016<4:TIAACM>2.0.CO;2](http://doi.org/10.1130/1052-5173(2006)016<4:TIAACM>2.0.CO;2).

1222

1223 Thomas, W.A. 2018. Tectonic inheritance at multiple scales during more than two complete Wilson  
1224 cycles recorded in eastern North America. *Geological Society, London, Special Publications*, **470**,  
1225 SP470.474, <http://doi.org/10.1144/SP470.4>.

1226

1227 Tommasi, A. & Vauchez, A. 2001. Continental rifting parallel to ancient collisional belts: an effect of  
1228 the mechanical anisotropy of the lithospheric mantle. *Earth and Planetary Science Letters*, **185**, 199-  
1229 210, [http://doi.org/10.1016/S0012-821x\(00\)00350-2](http://doi.org/10.1016/S0012-821x(00)00350-2).

1230

1231 Tulloch, A., Mortimer, N., Ireland, T., Waight, T., Maas, R., Palin, M., Sahoo, T., Seebeck, H., *et al.*  
1232 2019. Reconnaissance basement geology and tectonics of South Zealandia. *Tectonics*, **0**,  
1233 <http://doi.org/10.1029/2018TC005116>.

1234  
1235 Tulloch, A.J. 1988. Batholiths, plutons, and suites: nomenclature for granitoid rocks of Westland—  
1236 Nelson, New Zealand. *New Zealand Journal of Geology and Geophysics*, **31**, 505-509,  
1237 <http://doi.org/10.1080/00288306.1988.10422147>.

1238  
1239 Tulloch, A.J., Kimbrough, D.L., Landis, C.A., Mortimer, N. & Johnston, M.R. 1999. Relationships  
1240 between the brook street Terrane and Median Tectonic Zone (Median Batholith): Evidence from  
1241 Jurassic conglomerates. *New Zealand Journal of Geology and Geophysics*, **42**, 279-293,  
1242 <http://doi.org/10.1080/00288306.1999.9514845>.

1243  
1244 Tulloch, A.J., Ramezani, J., Kimbrough, D.L., Faure, K. & Allibone, A.H. 2009. U-Pb geochronology of  
1245 mid-Paleozoic plutonism in western New Zealand: Implications for S-type granite generation and  
1246 growth of the east Gondwana margin U-Pb geochronology of Paleozoic plutonism, New Zealand. *GSA  
1247 Bulletin*, **121**, 1236-1261, <http://doi.org/10.1130/B26272.1>.

1248  
1249 Uruski, C. 2015. The contribution of offshore seismic data to understanding the evolution of the New  
1250 Zealand continent. *Sedimentary Basins and Crustal Processes at Continental Margins: From Modern  
1251 Hyper-Extended Margins to Deformed Ancient Analogues*, **413**, 35-51,  
1252 <http://doi.org/10.1144/Sp413.1>.

1253  
1254 Uruski, C., Kennedy, C., Harrison, T., Maslen, G., Cook, R., Sutherland, R. & Zhu, H. 2007. Petroleum  
1255 potential of the Great South Basin, New Zealand—New seismic data improves imaging. *The APPEA  
1256 Journal*, **47**, 145-161, <http://doi.org/https://doi.org/10.1071/AJ06008>.

1257  
1258 Uruski, C.I. 2010. New Zealand's deepwater frontier. *Marine and Petroleum Geology*, **27**, 2005-2026,  
1259 <http://doi.org/https://doi.org/10.1016/j.marpetgeo.2010.05.010>.

1260  
1261 Van Buer, N.J., Miller, E.L. & Dumitru, T.A. 2009. Early Tertiary paleogeologic map of the northern  
1262 Sierra Nevada batholith and the northwestern Basin and Range. *Geology*, **37**, 371-374,  
1263 <http://doi.org/10.1130/g25448a.1>.

1264  
1265 Vasconcelos, D.L., Bezerra, F.H.R., Medeiros, W.E., de Castro, D.L., Clausen, O.R., Vital, H. & Oliveira,  
1266 R.G. 2019. Basement fabric controls rift nucleation and postrift basin inversion in the continental  
1267 margin of NE Brazil. *Tectonophysics*, **751**, 23-40,  
1268 <http://doi.org/https://doi.org/10.1016/j.tecto.2018.12.019>.

1269  
1270 Walsh, J.J. & Watterson, J. 1991. Geometric and kinematic coherence and scale effects in normal  
1271 fault systems. *Geological Society, London, Special Publications*, **56**, 193-203,  
1272 <http://doi.org/https://doi.org/10.1144/GSL.SP.1991.056.01.13>.

1273  
1274 Walsh, J.J., Nicol, A. & Childs, C. 2002. An alternative model for the growth of faults. *Journal of  
1275 Structural Geology*, **24**, 1669-1675, [http://doi.org/https://doi.org/10.1016/S0191-8141\(01\)00165-1](http://doi.org/https://doi.org/10.1016/S0191-8141(01)00165-1).

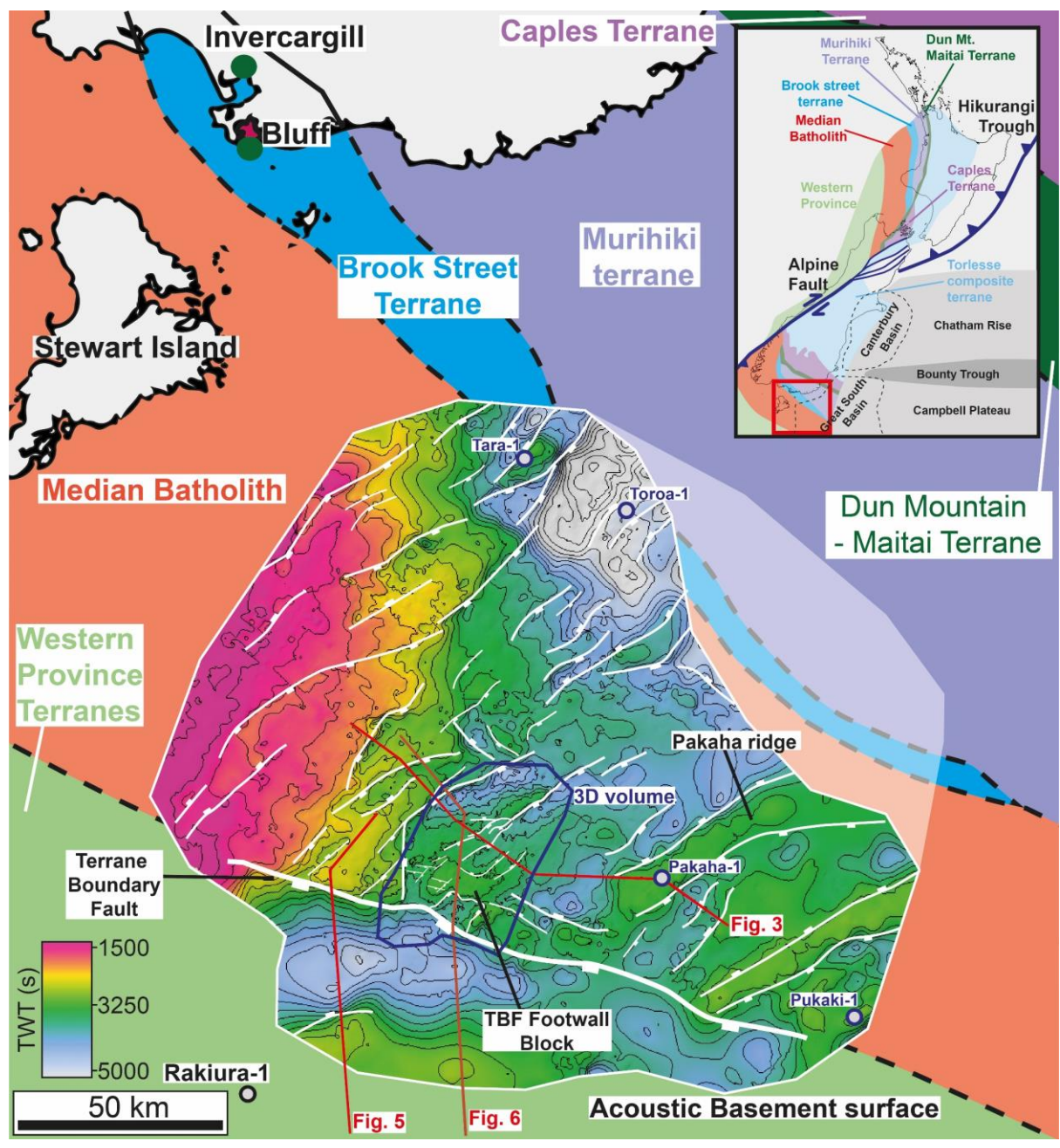
1276  
1277 Walsh, J.J., Watterson, J., Childs, C. & Nicol, A. 1996. Ductile strain effects in the analysis of seismic  
1278 interpretations of normal fault systems. *Geological Society, London, Special Publications*, **99**, 27,  
1279 <http://doi.org/10.1144/GSL.SP.1996.099.01.04>.

- 1280  
1281 Walsh, J.J., Bailey, W.R., Childs, C., Nicol, A. & Bonson, C.G. 2003. Formation of segmented normal  
1282 faults: a 3-D perspective. *Journal of Structural Geology*, **25**, 1251-1262,  
1283 [http://doi.org/https://doi.org/10.1016/S0191-8141\(02\)00161-X](http://doi.org/https://doi.org/10.1016/S0191-8141(02)00161-X).
- 1284  
1285 Wang, C.-Y., Okaya, D.A., Ruppert, C., Davis, G.A., Guo, T.-S., Zhong, Z. & Wenk, H.-R. 1989. Seismic  
1286 reflectivity of the Whipple Mountain shear zone in southern California. *Journal of Geophysical*  
1287 *Research: Solid Earth*, **94**, 2989-3005, <http://doi.org/10.1029/JB094iB03p02989>.
- 1288  
1289 Wannamaker, P.E., Caldwell, T.G., Jiracek, G.R., Maris, V., Hill, G.J., Ogawa, Y., Bibby, H.M., Bennie,  
1290 S.L., *et al.* 2009. Fluid and deformation regime of an advancing subduction system at Marlborough,  
1291 New Zealand. *Nature*, **460**, 733, <http://doi.org/10.1038/nature08204>  
1292 <https://www.nature.com/articles/nature08204#supplementary-information>.
- 1293  
1294 Wellman, H.W. 1953. Data for the study of recent and late Pleistocene faulting in the South Island of  
1295 New Zealand. *New Zealand Journal of Science and Technology*, **34 B**, 270-288.
- 1296  
1297 Wenker, S. & Beaumont, C. 2016. Effects of lateral strength contrasts and inherited heterogeneities  
1298 on necking and rifting of continents. *Tectonophysics*,  
1299 <http://doi.org/https://doi.org/10.1016/j.tecto.2016.10.011>.
- 1300  
1301 Whipp, P.S., Jackson, C.A.L., Gawthorpe, R.L., Dreyer, T. & Quinn, D. 2014. Normal fault array  
1302 evolution above a reactivated rift fabric; a subsurface example from the northern Horda Platform,  
1303 Norwegian North Sea. *Basin Research*, **26**, 523-549, <http://doi.org/10.1111/bre.12050>.
- 1304  
1305 Wilson, J.T. 1966. Did the Atlantic Close and then Re-Open? *Nature*, **211**, 676-681,  
1306 <http://doi.org/10.1038/211676a0>.

1307

## 1308 **Figures**

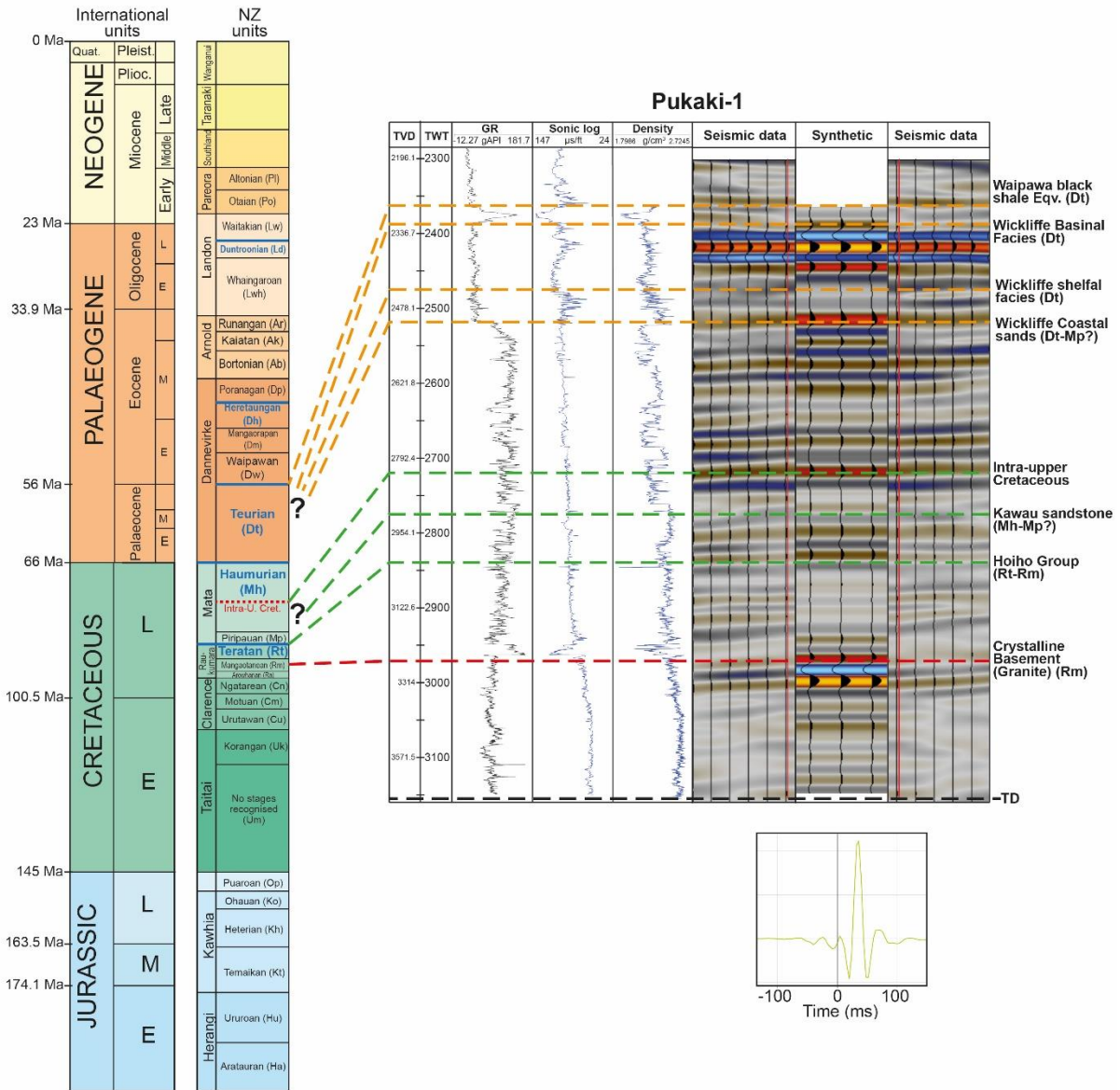
1309



1311

1312

1313 Figure 2

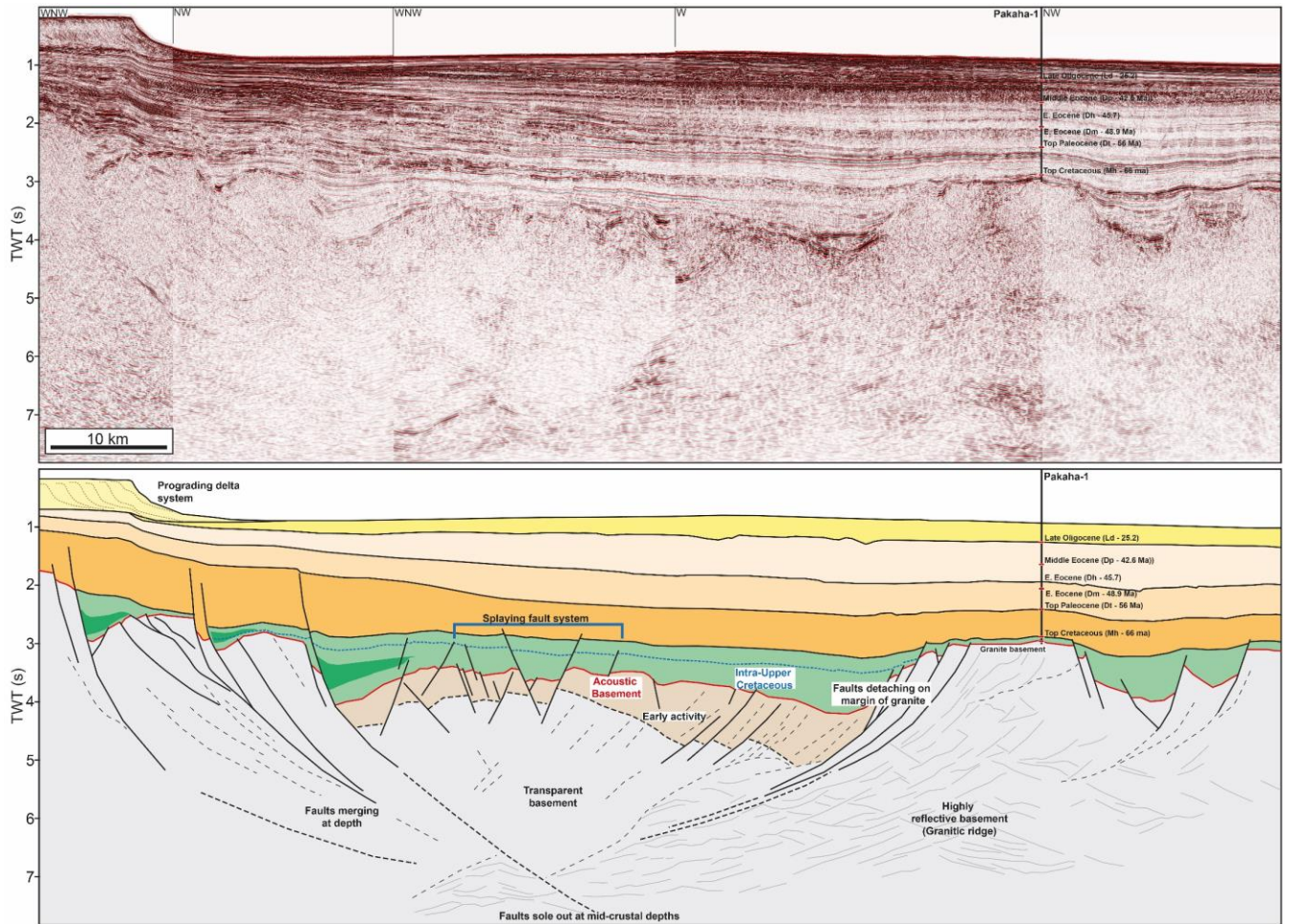


1314

1315

1316

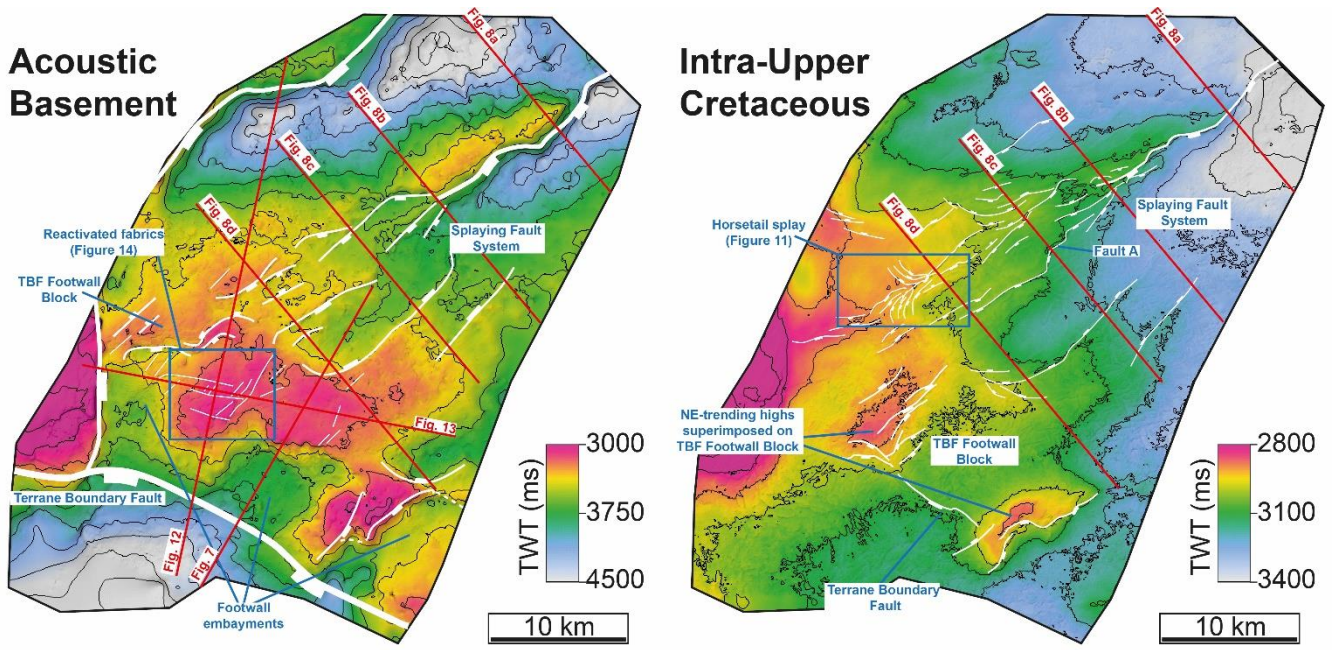
1317 Figure 3



1318

1319

1320 Figure 4

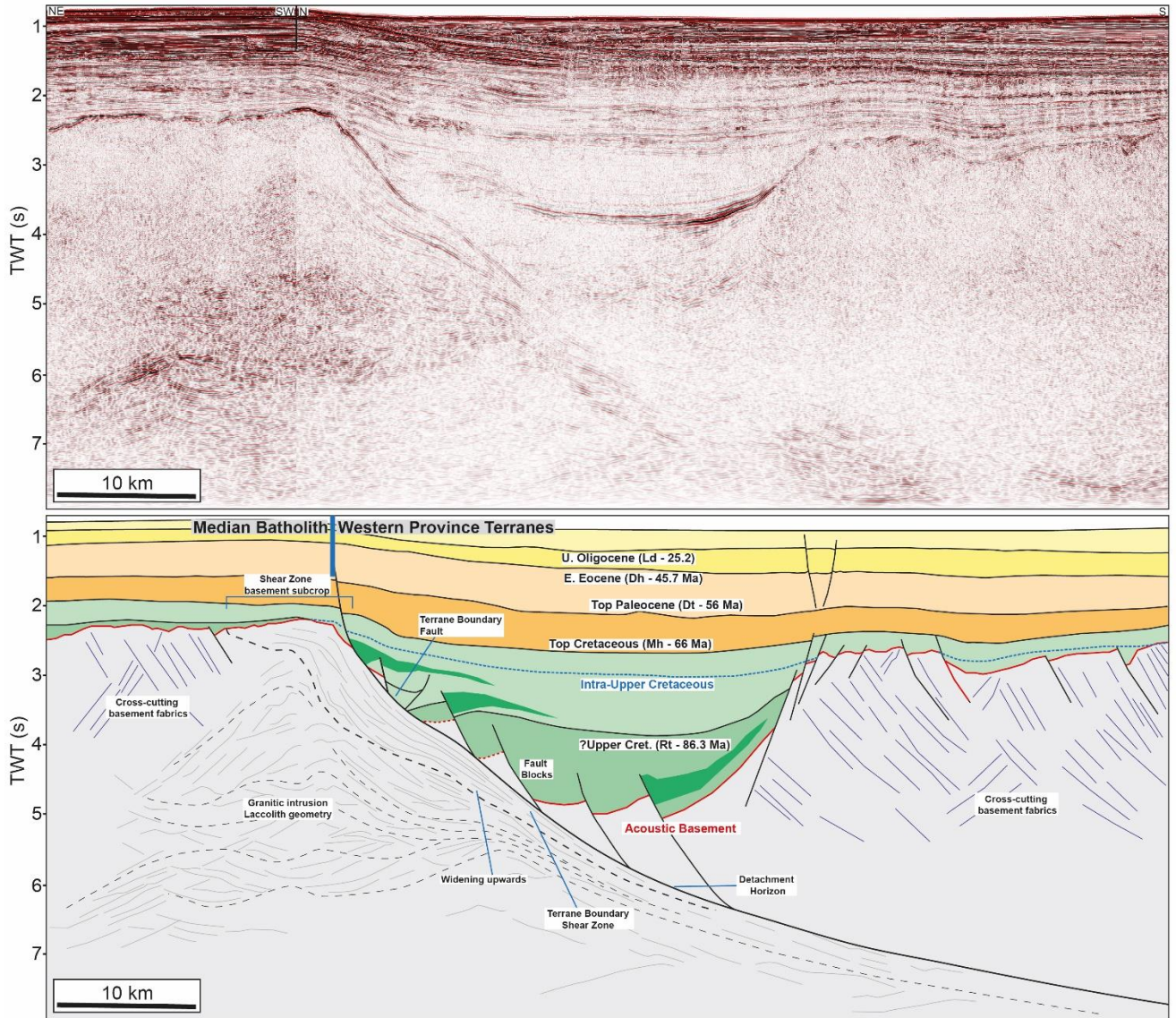


1321

1322



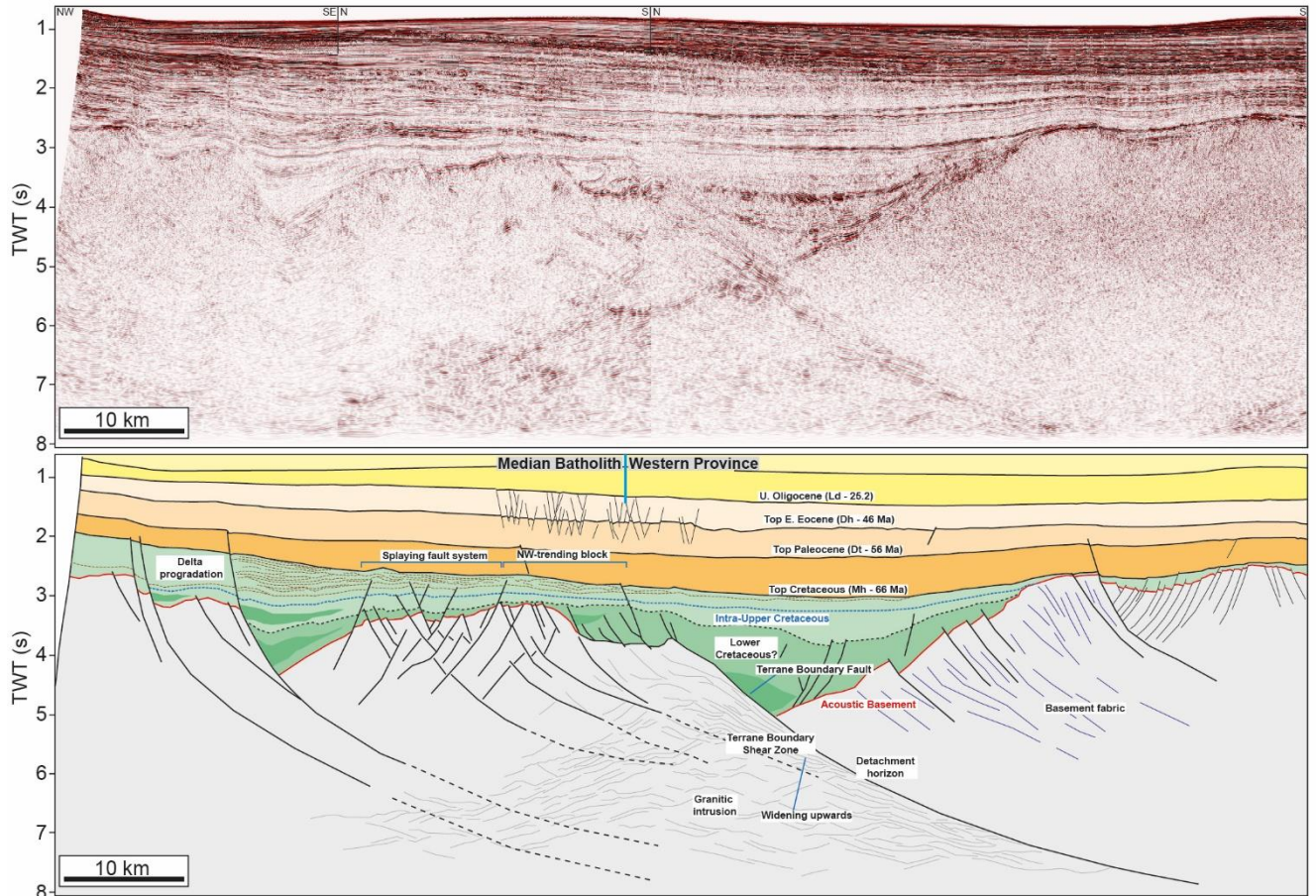
1323 Figure 5



1324

1325

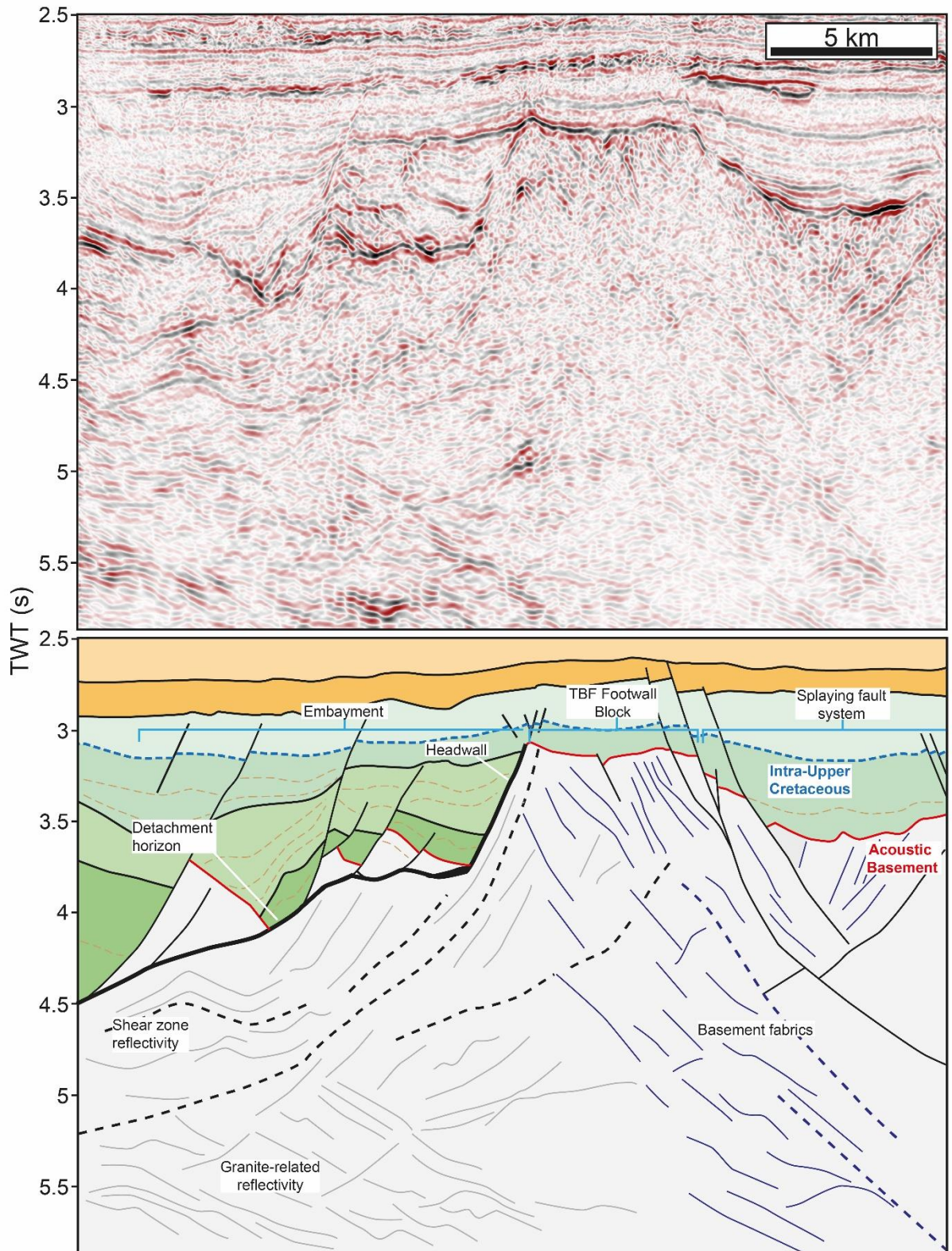
1326 Figure 6



1327

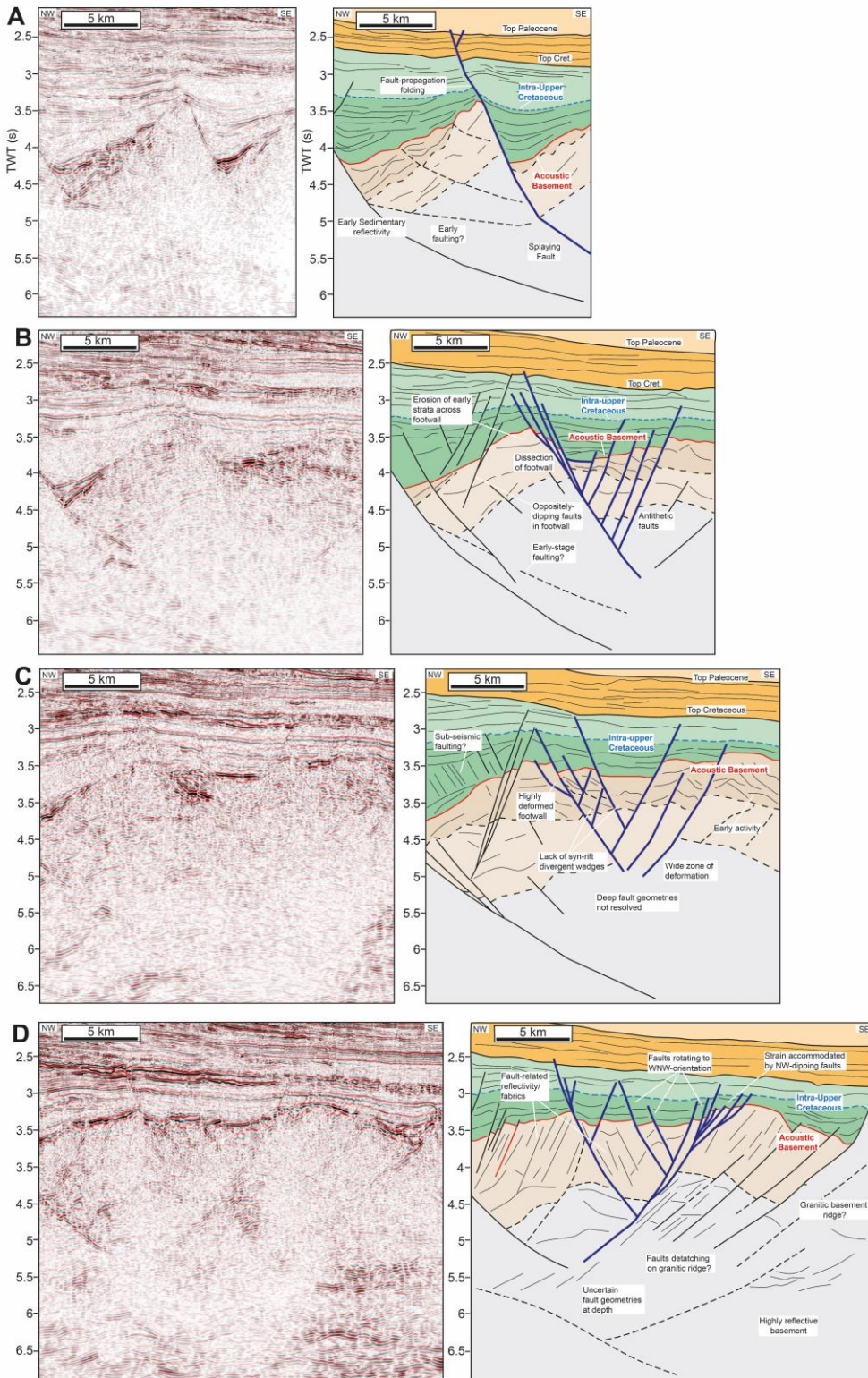
1328

1329 Figure 7

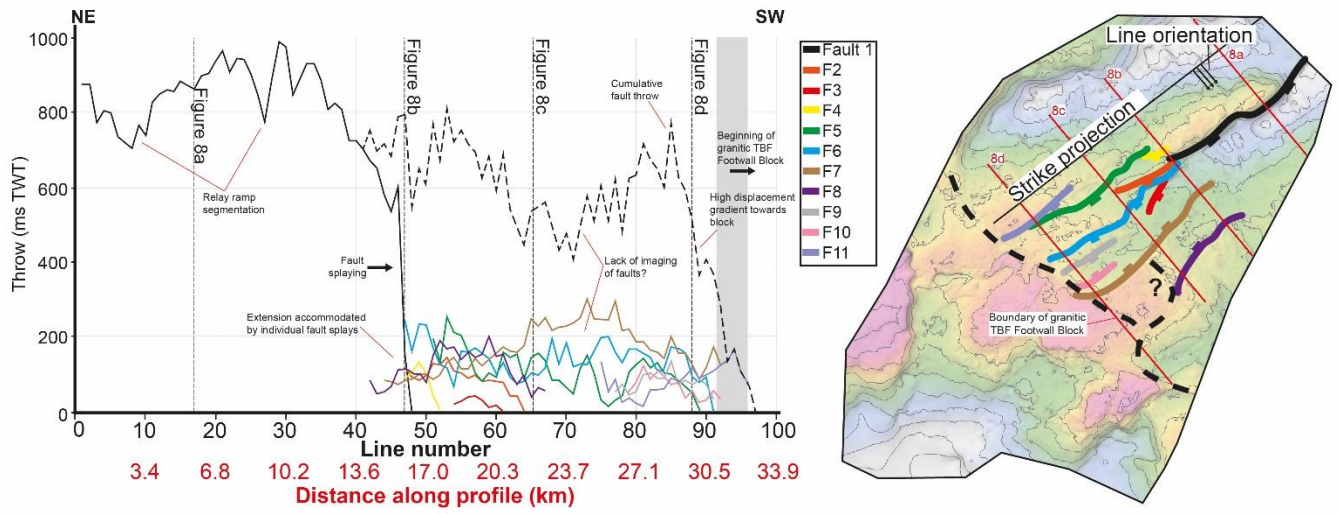


1330

1331



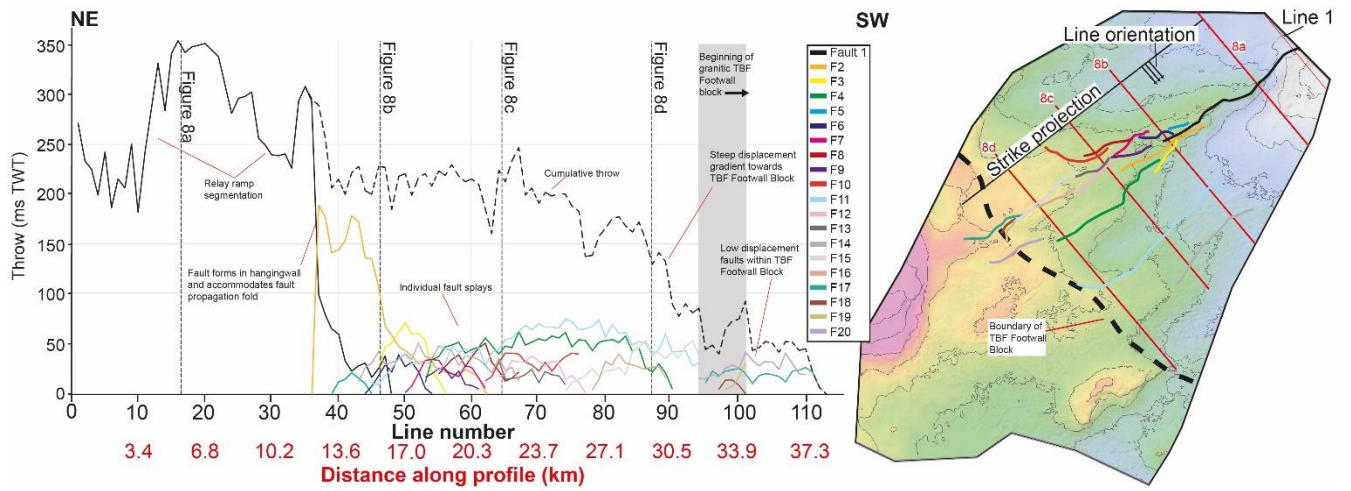
1335 Figure 9



1336

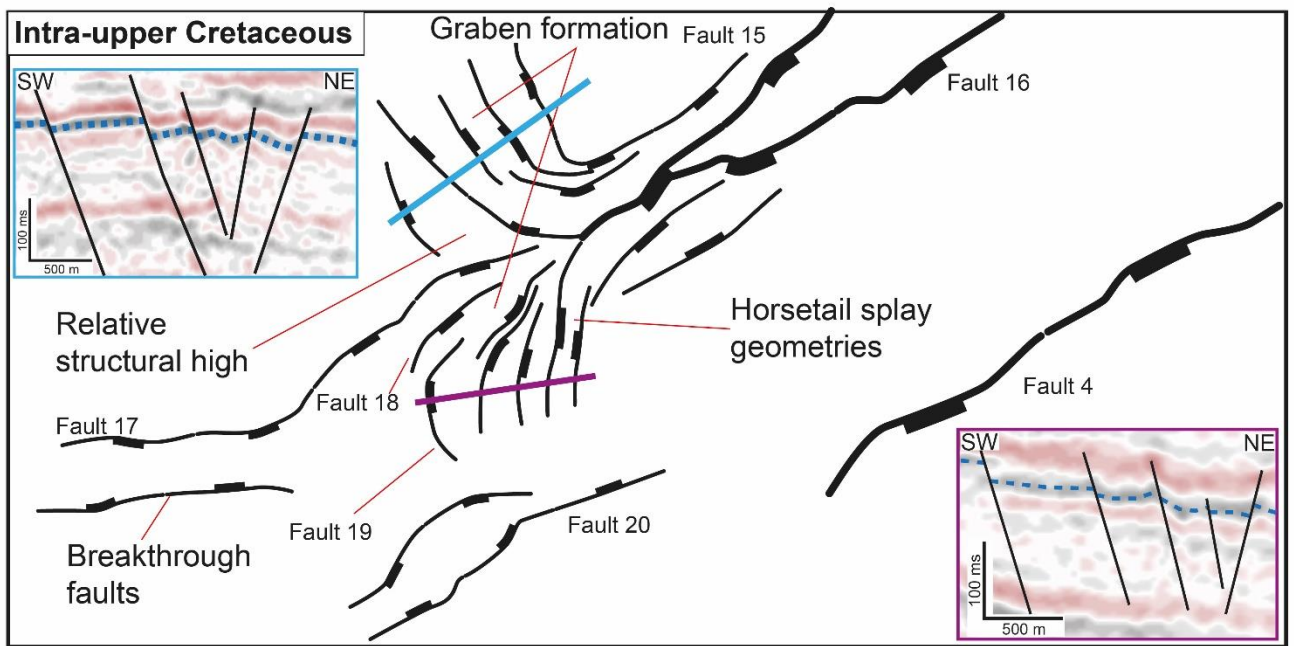
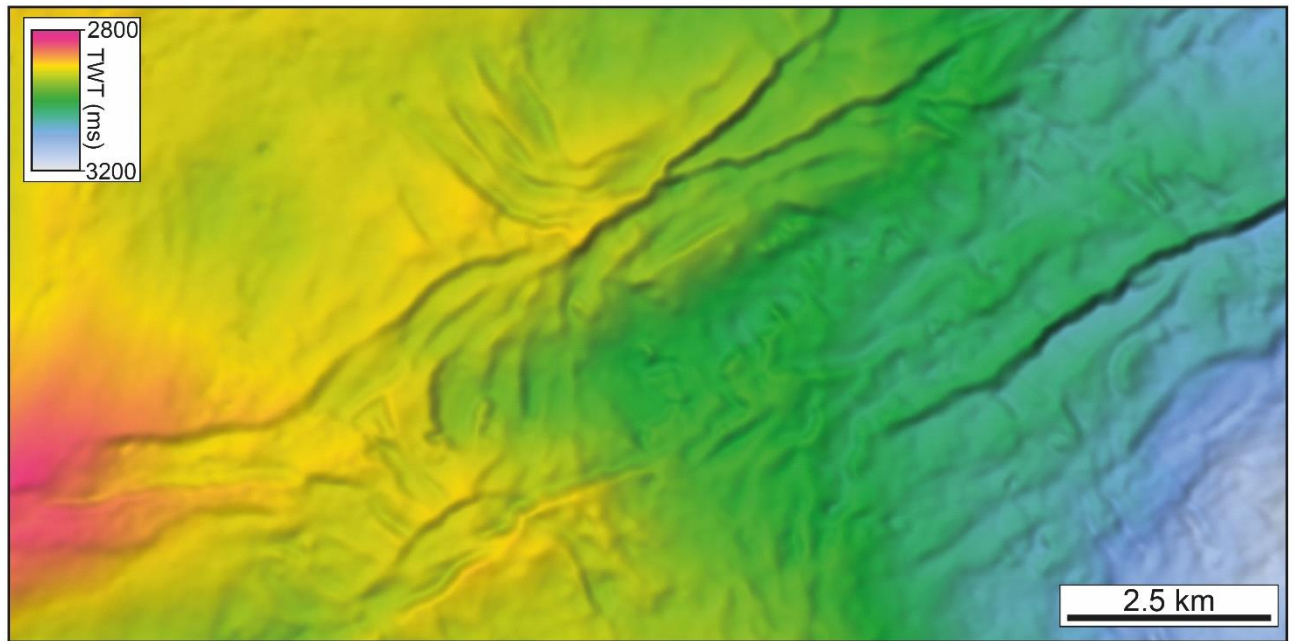
1337

1338 Figure 10



1339

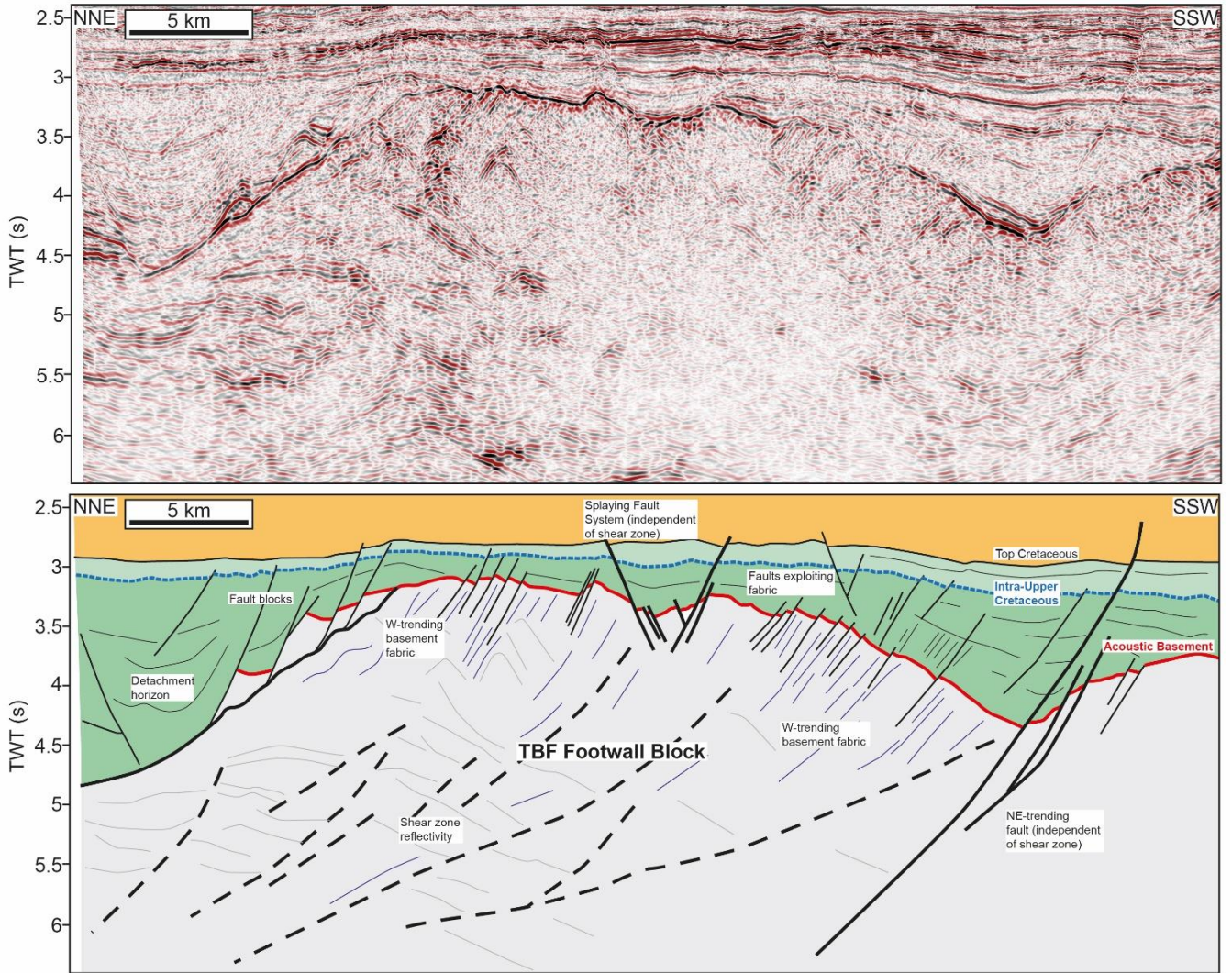
1340



1342

1343

1344 Figure 12

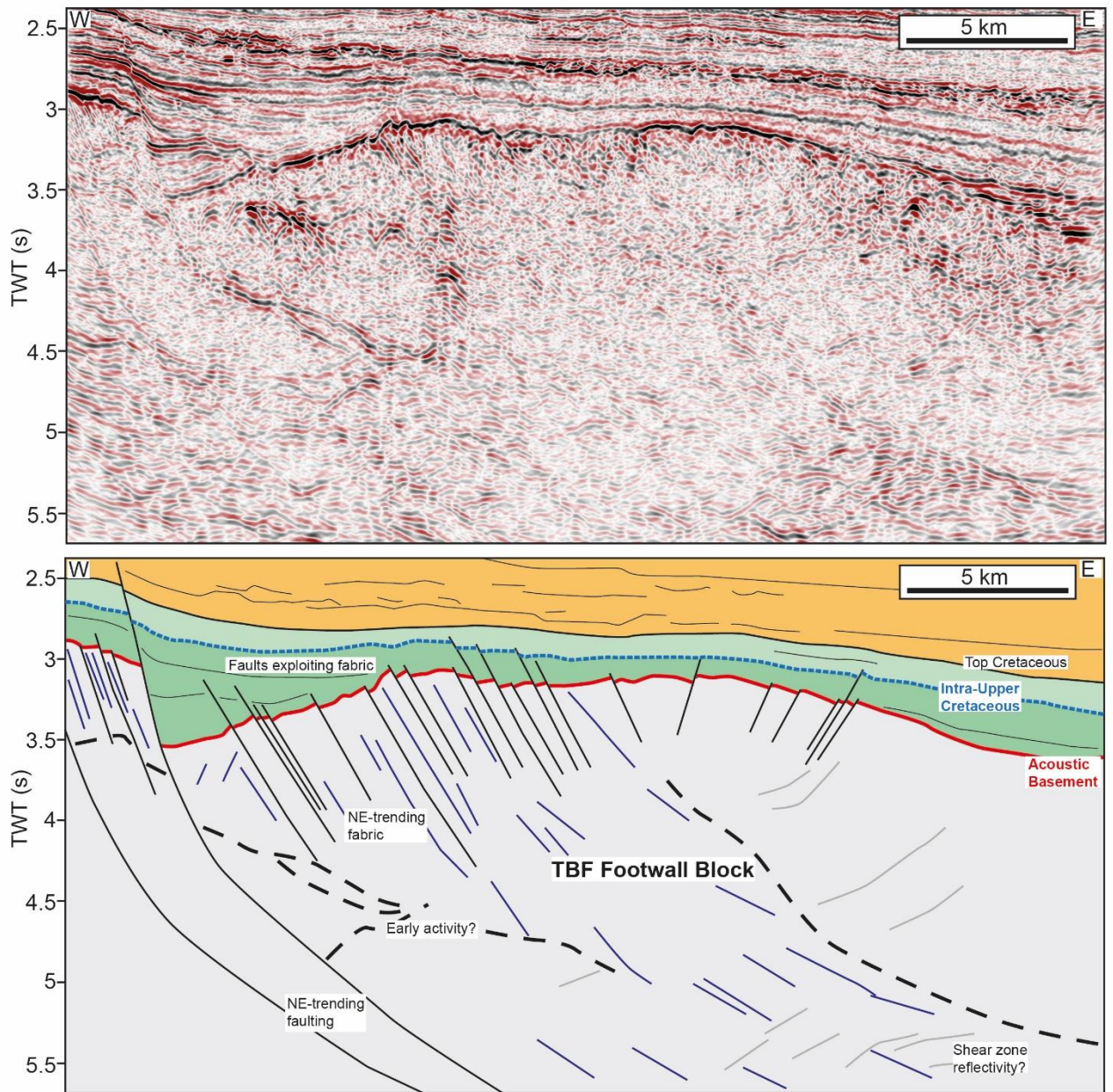


1345

1346



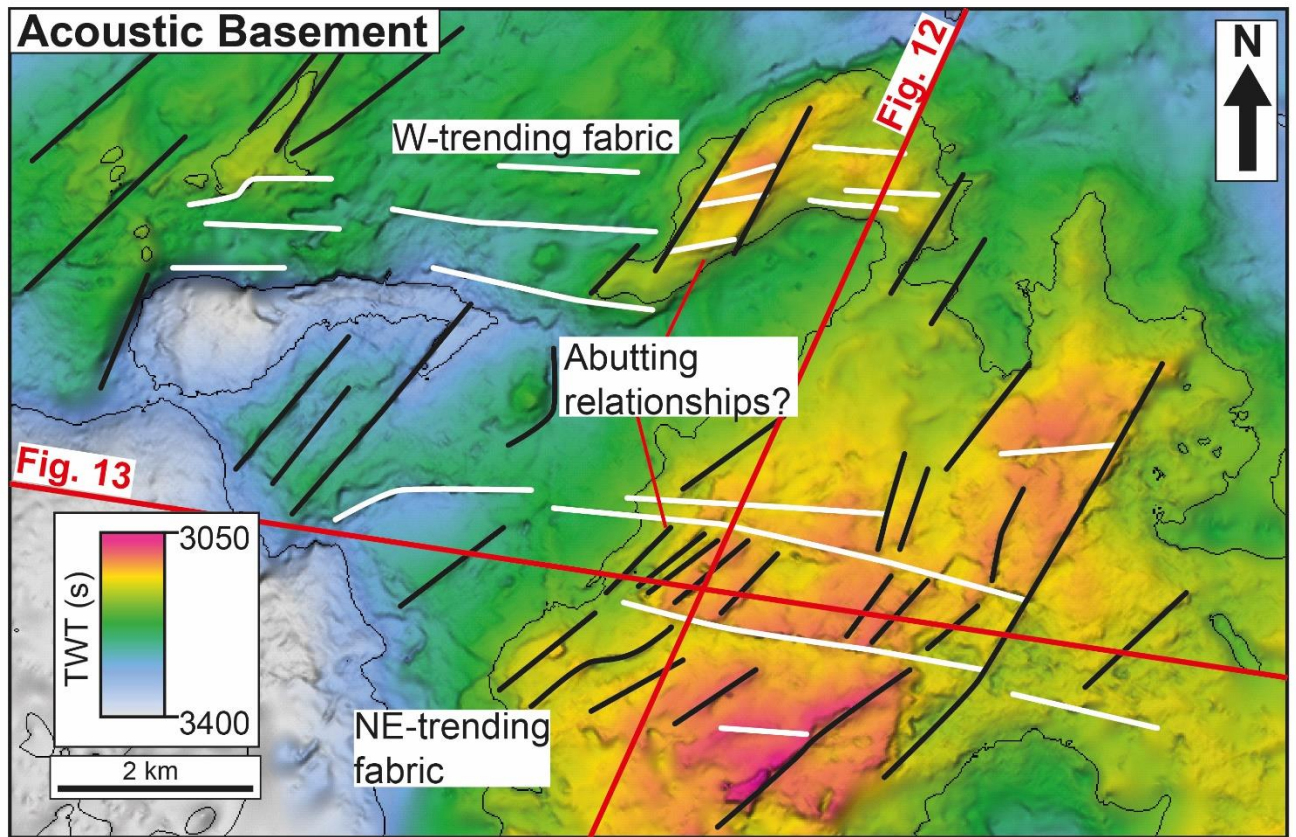
1347 Figure 13



1348

1349

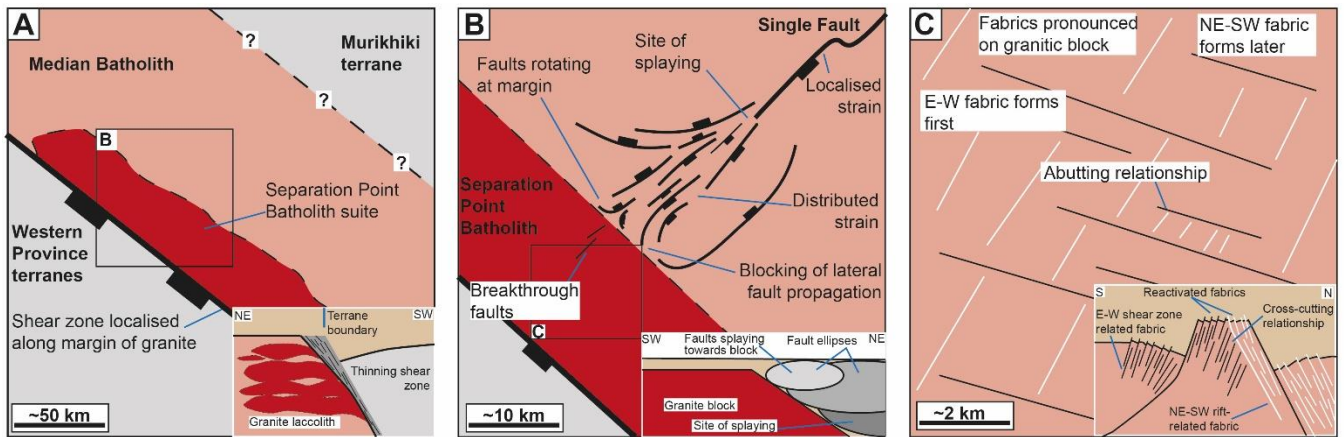
1350 Figure 14



1351

1352

1353 Figure 15



1354

1355

